



Dynamical Friction in Globular Cluster-rich Ultra-diffuse Galaxies: The Case of NGC5846-UDG1

Nitsan Bar¹ , Shany Danieli^{2,3,4} , and Kfir Blum¹ ¹ Department of Particle Physics and Astrophysics, Weizmann Institute of Science, Rehovot 7610001, Israel; nitsan.bar@weizmann.ac.il, kfir.blum@weizmann.ac.il² Department of Astrophysical Sciences, 4 Ivy Lane, Princeton University, Princeton, NJ 08544, USA; sdanieli@astro.princeton.edu³ Institute for Advanced Study, 1 Einstein Drive, Princeton, NJ 08540, USA

Received 2022 March 3; revised 2022 May 1; accepted 2022 May 17; published 2022 June 14

Abstract

Ultra-diffuse galaxies that contain a large sample of globular clusters (GCs) offer an opportunity to test the predictions of galactic dynamics theory. NGC5846-UDG1 is an excellent example, with a high-quality sample of dozens of GC candidates. We show that the observed distribution of GCs in NGC5846-UDG1 is suggestive of mass segregation induced by gravitational dynamical friction. We present simple analytic calculations, backed by a series of numerical simulations, that naturally explain the observed present-day pattern of GC masses and radial positions. Subject to some assumptions on the GC population at birth, the analysis supports the possibility that NGC5846-UDG1 resides in a massive dark matter halo. This is an example for the use of GC-rich systems as dynamical (in addition to kinematical) tracers of dark matter.

Unified Astronomy Thesaurus concepts: Low surface brightness galaxies (940); Dynamical friction (422); Globular star clusters (656); Galaxy dynamics (591); HST photometry (756); Dwarf galaxies (416); Galaxy formation (595)

1. Introduction

Dynamical processes shape galaxies and may provide constraints on the nature of dark matter (Binney & Tremaine 2008). In particular, dynamical friction (DF; Chandrasekhar 1943) can significantly impact the orbits of globular clusters (GCs) near the center of massive galaxies (Tremaine et al. 1975) or in the halos of dwarf and ultra-diffuse galaxies (e.g., Tremaine 1976; Sanchez-Salcedo et al. 2006; Nusser 2018; Dutta Chowdhury et al. 2020). The Fornax dwarf satellite galaxy, hosting five or six GCs, is a well-studied test case where DF should have imprinted itself in the galaxy. Indeed, it was argued long ago that the lack of a nuclear star cluster in Fornax is surprising and perhaps poses a puzzle, because the DF time for GC orbits appears to be short compared with the age of the system (Tremaine 1976). Several studies have revisited this “Fornax globular cluster timing problem”, primarily focusing on the possibility that the dark matter halo in Fornax is cored (Oh et al. 2000; Sanchez-Salcedo et al. 2006; Goerdt et al. 2006; Cole et al. 2012; Boldrini et al. 2020; Meadows et al. 2020; Shao et al. 2021; Bar et al. 2021). However, the number of GCs in Fornax, although large relative to other Milky Way dwarf satellites, may be too small to allow robust conclusions.

The potential to constrain dark matter via dynamical considerations motivates us to look for additional galaxies with a large population of GCs. This is timely in part due to recent studies of ultra-diffuse galaxies (UDGs), which often times host large numbers of GCs (van Dokkum et al. 2017, 2018; Lim et al. 2018; Shen et al. 2021). In this paper we consider NGC5846-UDG1 (UDG1 for short; Forbes et al. 2019, 2021; Müller et al. 2020, 2021; Danieli et al. 2022), that

recently attracted considerable attention.⁵ At a distance of ~ 25 Mpc, stellar luminosity of $\sim 6 \times 10^7 L_\odot$, and half-light radius $r_{\text{eff}} \sim 2$ kpc, UDG1 harbors some ~ 50 GC candidates, representing $\sim 10\%$ of the stellar mass at the preset day (Danieli et al. 2022).

The left panel of Figure 1 shows the V-band Hubble Space Telescope (HST) WFC3/UVIS image of UDG1 and its nearby field, adapted from Danieli et al. (2022). The right panel shows all compact sources that were selected as GC candidates based on the photometric selection criteria in Danieli et al. (2022). In this work we focus on a low contamination sample of GC candidates, consisting of the 33 $m_V < 25.0$ mag objects contained within $2r_{\text{eff}}$ (twice the Sérsic half-light radius of the stellar body; inner circle in Figure 1), which has a background contamination of about one object, estimated by comparison to the nearby field (Danieli et al. 2022). Spectroscopic information is available for 11 of these bright GCs (Müller et al. 2020).

It is noteworthy that most of the brighter GCs in the right panel of Figure 1 are concentrated in the region $r < r_{\text{eff}}$. To explore this further, in Figure 2 we show the luminosity of this sample of GCs versus their projected distance from the center of the galaxy. The data shows a clear trend: more luminous GCs are on average closer to the center of the galaxy. We estimate a p -value of about 1% for the hypothesis that the data is a chance fluctuation and that there is no mass segregation (see Appendix A). This luminosity or mass segregation calls for a quantitative dynamical explanation.

In this paper we show that this explanation can be naturally provided by DF. The deceleration experienced by a GC due to DF in a galactic halo is roughly proportional to the GC mass m_* . Therefore, more-massive GCs inspiral closer to the center of the galaxy, resulting in mass segregation. This simple picture can be expected to hold over an intermediate duration of time: long enough to enable DF to act, but short enough so that GC

⁴ NASA Hubble Fellow.

Original content from this work may be used under the terms of the [Creative Commons Attribution 4.0 licence](https://creativecommons.org/licenses/by/4.0/). Any further distribution of this work must maintain attribution to the author(s) and the title of the work, journal citation and DOI.

⁵ See also NGC1052-DF2, with 10 spectroscopically confirmed GCs, which was studied in Nusser (2018) and in Dutta Chowdhury et al. (2019, 2020).

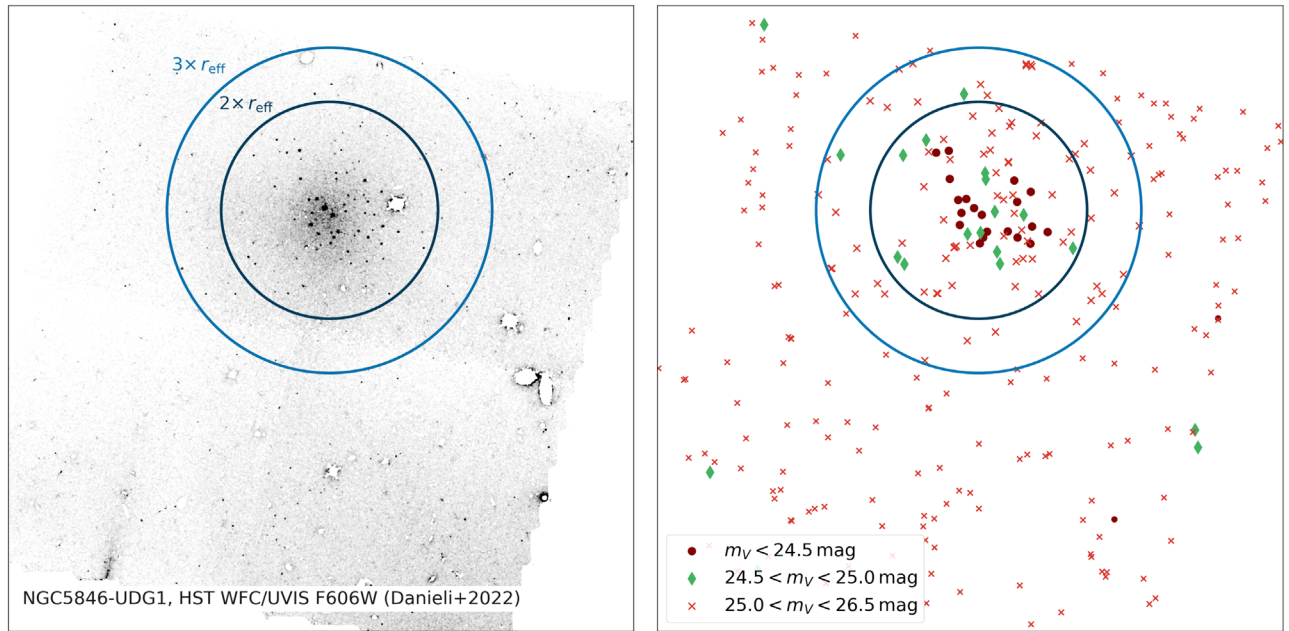


Figure 1. Left: reproduction of V-band data obtained in Danieli et al. (2022) using the Hubble Space Telescope WFC3/UVIS camera, containing UDG1 and a nearby field (postselection criteria described in Danieli et al. 2022). Circles represent $2r_{\text{eff}}$ and $3r_{\text{eff}}$ of the stellar light profile, with r_{eff} the Sérsic radius. Right: a scatterplot of objects from the left panel, divided into magnitude bins. The magnitude bins for objects at $m_V < 25.0$ mag are relatively clean from background contamination. In comparison, contamination is significant for the bin $25.0 < m_V < 26.5$ mag. In our main analysis, we primarily use the $r < 2r_{\text{eff}}$ data of the $m_V < 25.0$ mag bins. We present a preliminary analysis of the $25.0 < m_V < 26.5$ mag bin in Appendix D, showing that the faint objects also exhibit radial clustering above the background, comparable to the stellar body.

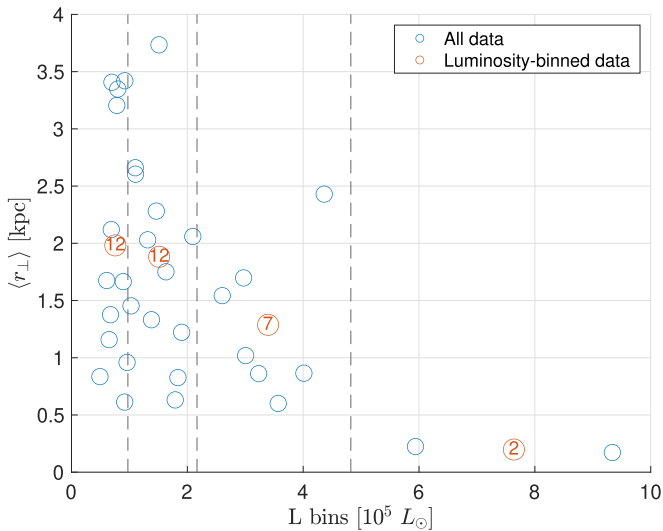


Figure 2. Red circles with numbers: circle position along the y-axis shows the average projected distance $\langle r_{\perp} \rangle$, for GCs belonging to luminosity bins (x-axis) marked by vertical dashed lines. Numbers indicate the number of GCs per bin. The luminosity bins are equispaced in log scale. We assume distance $D = 26.5$ Mpc. Blue circles show the unbinned data, comprised of the $m_V < 25.0$ mag objects inside $r < 2r_{\text{eff}}$ in Figure 1. Fainter objects (with significant background contamination) are not shown here; in Appendix D we find that the faint object population yields $\langle r_{\perp} \rangle \sim 2 \div 2.5$ kpc, consistent with the pattern of the $m_V < 25.0$ mag sample.

mergers do not convert a large fraction of the total mass in GCs into a nuclear cluster. As we will demonstrate, using more detailed analytic estimates as well as a suite of numerical simulations, UDG1 as we view it today may indeed be in this intermediate stage.

The paper is organized as follows. In Section 2 we discuss dynamical effects that shape the GC population in UDG1 and

similar galaxies. In Section 3 we recapitulate observational studies of UDG1, and define benchmark mass models. In Section 4 we set up and study N -body simulations, in which some dynamical effects (notably DF and GC mass loss) are modeled semianalytically. In Section 5 we discuss the results. We conclude in Section 6.

We reserve some details to the [Appendices](#). In Appendix A we show the sensitivity of the results to GC selection criteria and the significance of the mass segregation trend. In Appendix B we derive two-body relaxation in an external potential. In Appendix C we discuss projection effects. In Appendix D we present a preliminary analysis of the faintest GC candidates in UDG1. In Appendix E we present a number of convergence and stability tests of the simulations.

2. Back of the Envelope Analytic Estimates

The orbits of GCs traversing a background medium are processed by DF (Chandrasekhar 1943). A convenient expression for the timescale of DF is presented in Hui et al. (2017),

$$\tau_{\text{DF}} \equiv \frac{v^3}{4\pi G^2 \rho m_* C} \approx 2 \left(\frac{v}{10 \frac{\text{km}}{\text{sec}}} \right)^3 \frac{3 \times 10^6 \frac{M_{\odot}}{\text{kpc}^3}}{\rho} \frac{3 \times 10^5 M_{\odot}}{m_*} \frac{2}{C} \text{ Gyr}, \quad (1)$$

where ρ is the density of the medium inducing the DF, m_* is the GC mass, and C is a dimensionless factor encoding the details of the velocity dispersion of the medium and a Coulomb logarithm. For some dwarf galaxies and UDGs, $\tau_{\text{DF}} \lesssim 10$ Gyr, meaning that DF should be effective over the life of the galaxy. This was noticed long ago for the Fornax dwarf spheroidal

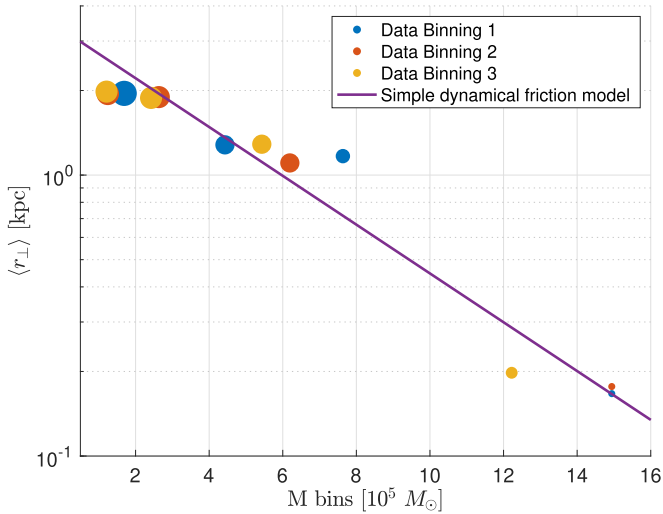


Figure 3. The data from Figure 2, overlaid with the simple dynamical friction model captured by Equation (2). The results are shown with three different choices of binning in GC mass. Point size indicates the amount of GCs per bin. (The last two points on the right should overlap; their position was slightly displaced for clarity.)

satellite galaxy (Tremaine 1976) and more recently for NGC1052-DF2 (Nusser 2018; Dutta Chowdhury et al. 2019).⁶

UDG1 with its unusually large population of GCs is likely another system where DF is effective. The mass segregation observed in Figure 2 can be interpreted as a natural outcome of DF, because of the dependence $\tau_{\text{DF}} \propto 1/m_*$ in Equation (1) (neglecting logarithmic dependence on m_* , sequestered in C). To illustrate how the m_* scaling leads to mass segregation, consider a cored halo, for which τ_{DF} is independent of radial position to leading order (Bar et al. 2021). In such a system, a GC on a circular orbit that starts its life at radius r_0 , migrates during time t to a lower radius $r \approx r_0 \exp(-t/2\tau_{\text{DF}})$ (Bar et al. 2021). Accounting for projection and averaging over a population of GC orbits (see Equation (C1)), one finds

$$\ln \langle r_{\perp} \rangle_{\text{core}} = \ln \langle r_{0,\perp} \rangle_{\text{core}} - \frac{\Delta t}{2\tau_{\text{core}}^{(0)}} \frac{m_*}{m_*^{(0)}}, \quad (2)$$

where angle brackets denote population average.

Assuming that the orbit distributions of GCs of different masses start with the same average initial radius, the simple model in Equation (2) can be compared to data, with two free parameters: (i) the initial average projected radius, $\langle r_{0,\perp} \rangle_{\text{core}}$, and (ii) the core DF time measured in units of the age of the system, $\tau_{\text{core}}^{(0)}/\Delta t$, computed for a reference GC mass $m_*^{(0)}$.

In Figure 3 we compare this model to the data from UDG1. We set $\langle r_{0,\perp} \rangle_{\text{core}} = 3$ kpc, somewhat larger than the observed stellar average projected radius ≈ 2.1 kpc, and $\tau_{\text{core}}^{(0)}/\Delta t = (5 \text{ Gyr})/(10 \text{ Gyr})$, with $m_*^{(0)} = 5 \times 10^5 M_{\odot}$, amounting to

$$\tau_{\text{DF}} \approx 5 \frac{5 \times 10^5 M_{\odot}}{m_*} \text{ Gyr}. \quad (3)$$

To convert from GC luminosity to mass, we assume a mass-to-light ratio $m_* = 1.6(L_*/L_{\odot}) M_{\odot}$, following Müller et al. (2020).

⁶ See also Lotz et al. (2001) for a survey of GCs in dwarf elliptical galaxies in the Virgo cluster and Sánchez-Salcedo & Lora (2022) for an analysis of GCs in dwarf spheroidal and dwarf irregular galaxies.

The data in Figure 3 is shown for three different choices of binning in m_* .⁷

In the rest of this section we discuss a number of additional effects that are, to some extent, intertwined with DF. These include gravitational GC–GC interactions, GC mergers, deformation of the background stellar and dark matter halo and dynamical heating by GCs, and GC mass loss. Some of these effects are interesting and could, under specific circumstances, modify the simple DF analysis. We will include a treatment of all of these effects in the numerical simulations described in Section 4.

2.1. Mergers of GCs

A large density of GCs could lead to a high rate of GC–GC mergers. A crude estimate of the merger rate per GC is

$$\begin{aligned} \Gamma &\sim n_{\text{GC}} \sigma_I v \\ &\sim \frac{0.1}{10 \text{ Gyr}} \frac{n_{\text{GC}}}{\left[\frac{20}{\frac{4\pi}{3}(2 \text{ kpc})^3} \right]} \frac{\sigma_I}{\pi (20 \text{ pc})^2} \frac{v}{10 \frac{\text{km}}{\text{s}}}, \end{aligned} \quad (4)$$

where n_{GC} is the number density of GCs and σ_I is the merger cross section. Multiplying by the currently observed number of GCs yields ~ 3 mergers in UDG1.

The crude estimate above can be compared with results of numerical simulations performed in Dutta Chowdhury et al. (2020) for a different galaxy, NGC1052-DF2 (DF2). DF2 hosts a stellar core comparable to that of UDG1, but has only about a third of the number of GCs. Performing a simulation with “live” GCs (i.e., made of a collection of stars rather than a single object, so that GC collisions can be resolved in some detail), Dutta Chowdhury et al. (2020) found an average number of GC mergers in DF2, over 10 Gyr, of about 0.3 (at a rate of 0.03 Gyr^{-1}). Since the number of mergers $\propto n_{\text{GC}}^2$, this would be consistent with ~ 3 mergers in UDG1 over 10 Gyr. We note however that Dutta Chowdhury et al. (2020) used the observed present-day distribution of GCs in DF2 as initial conditions for their simulations. Therefore, they simulated the future of the GC system, and since DF causes the GC distribution to converge inward with time, it is likely that the (already small) reported merger efficiency was even smaller over a similar timescale in the past. In our work we will attempt to trace the history of the GC system in UDG1, so the initial conditions we select correspond to a GC system that is less dense than what is currently observed. Thus, the rate of mergers we find is indeed generically small.

In Section 4 we will discuss how we implement GC mergers in our simulations. We agree with the conclusions of Dutta Chowdhury et al. (2020) that DF enhances the GC merger rate, as an outcome of the increase of GC density with time.

It is tempting to speculate that the most luminous (and most centrally located) GCs of UDG1 (see Figure 2) could be the result of DF-induced mergers. A closely related hypothesis was brought up long ago in the context of nuclear clusters in other galaxies (Tremaine et al. 1975; Capuzzo-Dolcetta 1993; Ostriker & Gnedin 1997; Capuzzo-Dolcetta & Tesseri 1997; Gnedin et al. 2014; Arca-Sedda & Capuzzo-Dolcetta 2014a). We return to this possibility later on.

⁷ The bin settings are (1) $M/(10^5 M_{\odot}) = [0.7, 3, 6, 12, 25]$, (2) $M/(10^5 M_{\odot}) = \exp[\ln 0.7: 0.8: \ln 30]$, and (3) $M/(10^5 M_{\odot}) = \exp[\ln 0.7: 0.9: \ln 30]$.

2.2. Mass Loss of GCs

Old massive ($\gtrsim 10^5 M_\odot$) GCs are expected to have lost a part of their mass over their life due to stellar evolution and dynamical processes (for a recent review, see Krumholz et al. 2019). We estimate the importance of this effect for our analysis, adopting a phenomenological approach. We treat GCs as point masses, losing mass at a prescribed rate without modeling the “microphysics” of the process. As a benchmark, we adopt the mass loss rate from Shao et al. (2021) (see Figure C1 there).⁸ With this prescription, GCs lose $\sim 30\%$ of their initial mass over a short ~ 0.5 Gyr interval in an early phase, followed by a \sim Gyr intermediate phase of $\sim 20\%$ mass loss. The remainder ~ 10 Gyr is characterized by a slower steady mass loss of about 30% of the GC mass (compared to the beginning of that last phase).

Assuming that dynamical relaxation timescales are longer than ~ 0.5 Gyr (although see Section 2.3 for possible exceptions), it is a reasonable approximation to simply consider the initial GC distribution to be defined after the first brief mass loss episode. Therefore, it seems reasonable to assume a mass loss rate of $\dot{m}_* \sim -(m_*^{(0)}/3)/10$ Gyr, i.e., $m_*(t) = m_*^{(0)}[1 - \delta \times t/t_0]$ with $\delta = 1/3$, $t_0 = 10$ Gyr. In a simplified model like that leading to Equation (2), this can be roughly incorporated by using an “effective” GC mass $m_*^{(\text{eff})} \approx m_*^{(\text{obs})}(1 + \delta/2) \approx 1.2m_*^{(\text{obs})}$, where $m_*^{(\text{obs})}$ is the currently observed GC mass (neglecting mergers). This amounts to an effective τ_{DF} that is $\sim 20\%$ shorter compared to a naive expectation based on the currently observed GC masses. We thus expect that mass loss is not a crucial factor in the dynamics of UDG1. Nevertheless, for completeness, when we set up simulations in Section 4 we take this effect into account.

2.3. Relaxation of GCs between Themselves

Two-body relaxation between stars or star clusters is typically thought to be unimportant on the scales of galaxies (Binney & Tremaine 2008),⁹ but diffuse galaxies with a rich GC population may present a counterexample. Assume N GCs of equal masses spread over a radial scale R with velocity scale v , comprising a fraction f of the total mass within R (i.e., $f \equiv M_{\text{GCs}}/M$). It is straightforward to extend classic arguments (Binney & Tremaine 2008) to derive a two-body relaxation timescale (for details, see Appendix B)

$$t_{\text{relax}} \sim \frac{0.1N}{\ln \frac{N}{f}} \frac{1}{f^2} t_{\text{cross}} \sim 10 \frac{N}{30} \frac{R}{2 \text{ kpc}} \frac{10 \text{ km s}^{-1}}{v} \left(\frac{0.1}{f} \right)^2 \text{ Gyr}, \quad (5)$$

where $t_{\text{cross}} \sim R/v$. Here, the reference value chosen for v represents a somewhat extreme scenario in which the gravitational potential of UDG1 is dominated by the stellar mass. We note that the spectroscopic study of Forbes et al. (2021) reported a line-of-sight velocity dispersion $17 \pm 2 \text{ km s}^{-1}$, suggesting a

dark matter–dominated halo and yielding a long two-body relaxation timescale for GCs in UDG1.

Two-body relaxation of GCs assists DF in inducing mass segregation. In Appendix B we present an N -body simulation in a smooth external potential that demonstrates this effect.

As briefly reviewed in Section 2.2, GCs are expected to lose $\mathcal{O}(1)$ of their mass over their life. With this in mind, Danieli et al. (2022) pointed out that the GC population may have initially comprised an $\mathcal{O}(1)$ fraction of the stellar mass in UDG1. This scenario could make two-body relaxation surprisingly efficient, if, in addition, the total halo mass of (and therefore velocity dispersion in) UDG1 is small. To see this, note that inserting $f \approx 0.5$ (à la the GC-dominance hypothesis of Danieli et al. 2022) along with $v \approx 10 \text{ km s}^{-1}$ (low mass / no dark matter hypothesis) into Equation (5) yields $t_{\text{relax}} \sim 0.5$ Gyr, a short relaxation time that could in principle affect the GC distribution at a noticeable level even during the brief initial mass loss phase of the GCs.¹⁰ If the halo is dark matter dominated (as supported by the spectroscopic study of Forbes et al. 2021), then $f \approx 0.5$ along with $v \approx 20 \text{ km s}^{-1}$ gives $t_{\text{relax}} \sim 5$ Gyr, making two-body relaxation relatively unimportant.

Put in a wider scope, these estimates suggest that there may be regions in “parameter space” of ultra-diffuse galaxies where two-body relaxation of GCs could be important.

Lastly, although we focused on the implications of two-body relaxation on the scale of an entire galaxy, the effect can manifest in part of a galaxy. Consider the possibility that $\mathcal{O}(10)$ GCs are driven by DF close the galactic center and stall there, e.g., due to core stalling (Read et al. 2006). Repurposing Equation (5) for this case, we find

$$t_{\text{relax}} \sim 0.3 \frac{N}{10} \frac{R}{1 \text{ kpc}} \frac{20 \text{ km s}^{-1}}{v} \left(\frac{0.2}{f} \right)^2 \text{ Gyr}. \quad (6)$$

Here values are motivated by UDG1 (see Section 3). The short relaxation time that we find suggests that even if DF becomes ineffective due to core stalling, mass segregation of GCs may proceed due to their N -body interaction, potentially allowing the formation of a nucleus.

3. Observational Constraints and Mass Models of UDG1

In this section we summarize observational constraints on UDG1, and describe halo mass models that we will use in numerical simulations.

Similar to Danieli et al. (2022), we adopt a distance of $D = 26.5 \pm 0.8$ Mpc to UDG1, based on the distance to the NGC5846 group, reported in Kourkchi & Tully (2017). Note that the association of UDG1 with the NGC5846 galaxy is not guaranteed and may perhaps be disfavored from kinematical measurements; Forbes et al. (2021) reports a radial velocity $2167 \pm 2 \text{ km s}^{-1}$ to UDG1, whereas NGC5846 galaxy was measured at $1712 \pm 5 \text{ km s}^{-1}$ (Cappellari et al. 2011). A radial-velocity difference of $\approx 455 \text{ km s}^{-1}$ is rather high for a satellite. We note that the trend seen in Figure 2 is qualitatively insensitive to the distance estimate, although detailed constraints on the galaxy halo could be affected. For example, since $r_\perp \propto D$ and $m_* \propto D^2$, within the scope of a simple analysis as in Figure 3 we can estimate that a 10% (20%)

⁸ Strictly speaking, the results there are reported around $2 \times 10^5 M_\odot$ whereas our analysis extends to larger GC masses, which are expected to lose a smaller mass fraction. We neglect this complication in the following.

⁹ Except very near galactic centers or for some candidates of dark matter (Hernandez et al. 2004; Hui et al. 2017; Bar-Or et al. 2019).

¹⁰ This scenario requires that most of the GCs were formed nearly at the same time, and no more than a few 100 Myr apart.

uncertainty on D yields an $\approx 20\%$ (40%) uncertainty on the DF timescale $\tau_{\text{core}}^{(0)}$ (with larger distances implying smaller DF).

The stellar luminosity was found to be well described by a Sérsic profile with index $n = 0.61$, half-light radius $R_e = 1.9$ kpc, and luminosity $L_V = 0.6 \times 10^8 L_\odot$ (Danieli et al. 2022).

UDG1 was noted for its large GC content (Müller et al. 2021, 2020; Forbes et al. 2021). The highest quality photometric data of these GCs were obtained using two-orbit WFC3/UVIS observations of the Hubble Space Telescope (Danieli et al. 2022). The compact objects catalog was processed into different populations corresponding to different selection criteria of magnitude, angular size, position, and color. Here we primarily adopt the two sets in the magnitude range $21 \lesssim m_V \lesssim 25$ due to their high quality and low contamination (about 1 expected object out of 33 in $r < 2R_e$, based on a nearby background field; see right panel of Figure 1). We note that our results are insensitive to the photometric selection criteria, as discussed in Appendix A.

At the faint end, $25 \lesssim m_V \lesssim 26.5$, the catalog suffers larger contamination (about 24 expected objects out of 43). We refrain from using it in our main analysis, but note that it can be useful in principle within a more comprehensive statistical analysis. We show a preliminary analysis in Appendix D.

Spectroscopic studies of UDG1 have confirmed the membership of 11 GCs in the galaxy (Müller et al. 2020; Forbes et al. 2021). Furthermore, Forbes et al. (2021) reported a GC line-of-sight velocity dispersion $\sigma_{\text{LOS}} = 17 \pm 2$ km s $^{-1}$, implying that dynamics are dominated by dark matter. In what follows we describe two dark matter–dominated mass models that roughly saturate the reported σ_{LOS} from Forbes et al. (2021), and one mass model that neglects dark matter altogether.

Stars A mass model following the observed stellar luminosity, adopting $M/L_V = 2M_\odot/L_\odot$ following Müller et al. (2020).

Burkert A mass model following Burkert (1995), $\rho = \rho_0 r_0^3 / [(r + r_0)(r^2 + r_0^2)]$. We set $r_0 = 2$ kpc and $\rho_0 = 1.66 \times 10^7 M_\odot/\text{kpc}^3$. The value we adopt for ρ_0 allows us to test a profile that is significantly more massive than the Stars profile, yet sufficiently dilute to have $\tau_{\text{DF}} \lesssim 10$ Gyr. In addition, this value is consistent with a velocity dispersion 17 ± 2 km s $^{-1}$ reported in Forbes et al. (2021; saturating the 1σ upper bound of Müller et al. 2020).

NFW A mass model following Navarro et al. (1997), $\rho = \rho_c \delta_c / [(r/R_s)(1 + r/R_s)^2]$. We set $R_s = 6$ kpc and $c = 6$, defined in the usual way in δ_c (Navarro et al. 1997). The predicted stellar kinematics in this model is comparable to those in the Burkert model. For reference, the virial mass of this model is $M_{200} = 200^{4\pi} \rho_c c^3 R_s^3 \approx 6 \times 10^9 M_\odot$.

In Figure 4 we show the density, line-of-sight velocity dispersion, DF timescale, and enclosed mass of the different mass models.

We can compare Figure 3 to the DF timescale in the bottom right of Figure 4. None of the models have constant τ_{DF} and ρ as a function of radius, as assumed in the toy model of Section 2, but the cored models (Stars and Burkert) come close. All of the models predict significant DF over a 10 Gyr

timescale, for GC orbits entering within a few kpc from the galaxy center.

4. Numerical Simulations

Our goal in the simulations is twofold. First, we aim to test the possibility that the apparent mass segregation in UDG1 is due to DF. A central unknown in the problem is the initial distribution of GCs; our first task is to explore a range of initial conditions and see if a reasonable starting distribution can naturally evolve into the observed one. Second, provided that we can indeed identify reasonable initial conditions for the distribution of GCs, consistent with current observations, we also aim to examine whether the GC data can discriminate between different halo models.

Predicting the long-term dynamics of a GC population in a galaxy like UDG1 would optimally involve direct integration of live GCs à la Dutta Chowdhury et al. (2020) with baryonic effects à la Shao et al. (2021) in high-resolution models of galaxies à la Meadows et al. (2020). Here, we take a more modest approach, simulating the N -body dynamics of GCs in a smooth external gravitational potential, adding DF using a semianalytic prescription (Petts et al. 2015; Bar et al. 2021).

4.1. Simulation Description

4.1.1. Outline

Dynamics. We set-up an N -body simulation, where each body represents a GC with a Plummer softening of $\epsilon = 7$ pc; i.e., the gravitational potential due to GC i is $\Phi_i(\mathbf{r}) = -GM_i / \sqrt{(\mathbf{r} - \mathbf{r}_i)^2 + \epsilon^2}$. The background halos of stars and dark matter are modeled by a smooth and static profiles corresponding to the models in Section 3, such that the background gravitational acceleration is modeled as $-GM(r)\hat{r}/r^2$.

DF is implemented using a deceleration term $-V/\tau_{\text{DF}}$. Specifically, we assume $C = \ln\Lambda[\text{erf}(X) - \exp(-X^2)2X/\sqrt{\pi}]$ (corresponding to a Maxwellian velocity distribution), where $X = V/\sqrt{2}\sigma$ and σ is the local velocity dispersion of the medium. The Coulomb logarithm $\ln\Lambda$ is modeled following Bar et al. (2021), where in the Stars and Burkert cases we select $\Lambda_{\text{ISO}} = 2V^2 r / (Gm_*)$, and for Navarro-Frenk-White (NFW) $\Lambda_{\text{NFW}} = b_{\text{max}}^2 \sigma^2 / (Gm_*)$ with $b_{\text{max}} = 0.5$ kpc. In both cases we use in practice $\ln\Lambda \rightarrow \frac{1}{2} \ln(1 + \Lambda^2)$ to regulate the logarithm when it becomes small and the treatment breaks down. As discussed in Bar et al. (2021), we can expect that the semianalytic procedure captures the correct numerical value of τ_{DF} to a factor of 2 or so.

As GCs inspiral inward due to DF, some of their orbital energy is transferred to and heats the background medium. Accurate modeling of this effect requires simulations that resolve the particles of the medium, which is beyond the scope of this work. Instead, to roughly model this effect, we limit DF to radii where $M_{\text{halo}}(r) - M_{\text{GC,enclosed}}(r)/2 > 0$. At radii $r < r_{\text{DF,crit}}$, where $r_{\text{DF,crit}}$ is defined by $M_{\text{halo}}(r) = M_{\text{GC,enclosed}}(r)/2$, we turn off the DF deceleration term. We update $r_{\text{DF,crit}}$ every 0.1 Gyr. For cored profiles (Stars and Burkert) we turn DF off at $r < 0.3R_e$ to mimic core stalling (Read et al. 2006; Kaur & Sridhar 2018; Meadows et al. 2020; Dutta Chowdhury et al. 2019).

We implement GC mergers using an effective merger criterion. The merger criterion we choose is the simultaneous fulfillment of the conditions $E_{12} \equiv \mu V_{12}^2/2 + U_{12}(r_{12}) < 0$ and

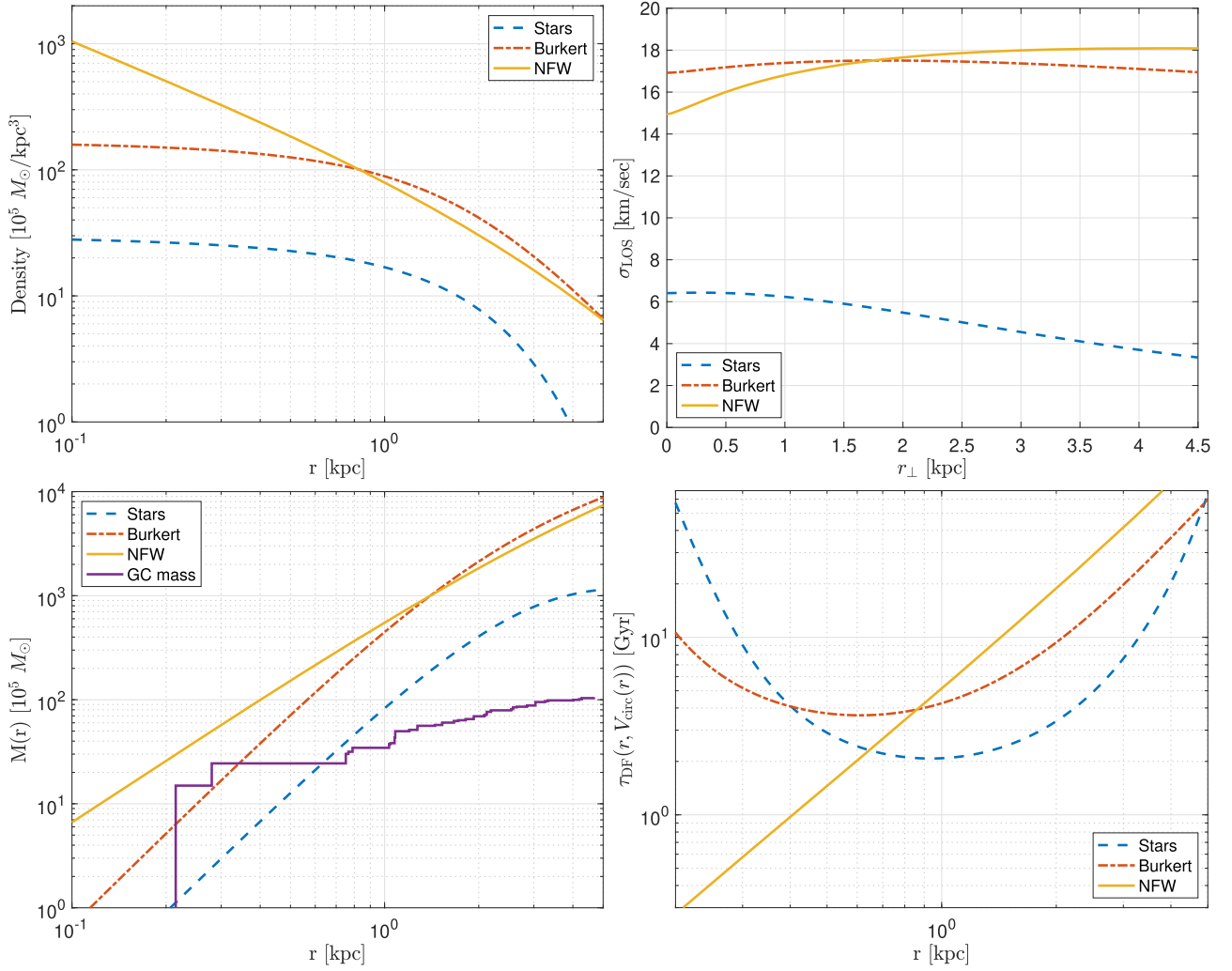


Figure 4. Properties of mass models that we use. Top left: mass density as a function of radius. Top right: expected line-of-sight velocity dispersion of the observed distribution of stars in Danieli et al. (2022) assuming isotropic velocity dispersion. Bottom right: the dynamical friction time evaluated with the velocity of a circular orbit for $m_* = 5 \times 10^5 M_\odot$, with Coulomb logarithms as described in Section 4.1.1. Bottom left: the enclosed mass of different models with a rough comparison to GCs mass profile, deprojected via the approximation $r = 1.25 \times r_\perp$ (see Equation (C3)).

$r < r_{\text{merger}} = 20 \text{ pc} \sim \text{few} \times \epsilon \text{ pc}$ (see Dutta Chowdhury et al. 2020). Here, $\mu = m_1 m_2 / (m_1 + m_2)$ is the reduced mass of the GC pair, $\mathbf{V}_{12} \equiv \dot{\mathbf{r}}_2 - \dot{\mathbf{r}}_1$ is the relative velocity, and $U_{12}(r_{12})$ is the relative potential. For point-like objects, $U_{12}(r_{12}) = -Gm_1 m_2 / r_{12}$. In general, $U_{12} = \frac{1}{2} \int (\rho_1 \Phi_2 + \rho_2 \Phi_1) d^3x$. For Plummer spheres with softening parameter ϵ we find that $U_{12} \approx -Gm_1 m_2 / (r_{12}^{2.11} + (1.7\epsilon)^{2.11})^{1/2.11}$ provides a very good approximation, which we adopt in the simulations.

Upon a merger, we assign the new combined GC mass $M = m_1 + m_2$, velocity $\mathbf{V} = (m_1 \mathbf{V}_1 + m_2 \mathbf{V}_2) / (m_1 + m_2)$, and location $\mathbf{R} = (\mathbf{r}_1 + \mathbf{r}_2) / 2$. This corresponds to a linear momentum-conserving “sticking” of GCs. Energy is not conserved in this process: we neglect mass loss during the merger. Thus, energy must be transferred to the internal dynamics of the GC, which we do not model.

We approximate the process of continuous mass loss by decreasing GC masses in time steps of 0.1 Gyr, following the mass loss trend described in Section 2.2.

Initial conditions. Simulated GCs start in random positions in an (on average) isotropic distribution. We test initial GC radial distributions which start off as a Sérsic profile with

different values of R_e . For simplicity, throughout we retain $n = 0.61$, similar to the stellar distribution.

We initiate the GC velocity distribution such that the radial distribution would remain stationary in the absence of DF, mass loss, and mergers (Binney & Tremaine 2008). Defining $\mathcal{E} = \Psi(r) - v^2/2$ (where $\Psi(r) \equiv -\Phi(r)$ taken conventionally to asymptote to zero at $r \rightarrow \infty$), the goal is to derive the distribution function $f(\mathcal{E})$ based on the number-density profile of GCs n_{GC} , under a spherically symmetric external potential Φ , satisfying the Poisson equation for the halo’s mass density $\nabla^2 \Phi = 4\pi G \rho_{\text{halo}}$. We adopt a numerically convenient expression for $f(\mathcal{E})$ (Magni 2015),

$$f(\mathcal{E}) = \frac{1}{\sqrt{8} \pi^2} \left[\frac{1}{\sqrt{\mathcal{E}}} \left(\frac{dn_{\text{GC}}}{d\Psi} \right) \Big|_{\Psi=0} + 2\sqrt{\mathcal{E}} \left(\frac{d^2 n_{\text{GC}}}{d\Psi^2} \right) \Big|_{\Psi=0} + 2 \int_0^{\mathcal{E}} d\Psi \sqrt{\mathcal{E} - \Psi} \frac{d^3 n_{\text{GC}}}{d\Psi^3} \right]. \quad (7)$$

For the density profiles that we use, the first two terms vanish, leaving

$$f(\mathcal{E}) \approx \frac{1}{\sqrt{2}\pi^2} \int_0^{\mathcal{E}} d\Psi \sqrt{\mathcal{E} - \Psi} \frac{d^3 n_{\text{GC}}}{d\Psi^3}. \quad (8)$$

We track the system during a 10 Gyr time period.

As discussed in the next subsection, we test different possibilities for the GC initial mass distribution. As a rule, we aim for an initial GC mass function that approximately matches the current GC mass function, accounting for mass loss.

Implementation. We implement the code in MATLAB using the ode45 solver, partially based on Pedcenko (2020). We use kpc-Gyr- $10^5 M_{\odot}$ units, for which $G = 0.449 \text{ kpc}^3/10^5 M_{\odot}/\text{Gyr}^2$ and $\text{kpc}/\text{Gyr} = 0.979 \text{ km s}^{-1}$. We use a constant time step of $dt = 2 \times 10^{-5} \times 2\pi R/v$ (R and v being characteristic radius and velocity scales of the system). This amounts to $dt \sim 10^{-5}$ Gyr.

Convergence. When DF, mergers, and mass loss are turned off, we find that energy is conserved to better than 1% over 10 Gyr.

Sensitivity to parameters. We tested the sensitivity of our results with respect to several parameters of the simulations, rerunning with (i) different Plummer softenings, $\epsilon = 4$ and 12 pc; (ii) different merger radii $r_{\text{merger}} = 10$ and 35 pc; (iii) unrestricted DF, i.e., without turning off DF for $r < 0.3R_e$ and $M_{\text{halo}} - M_{\text{GCs}}/2 < 0$; (iv) a higher central concentration initial GC distribution—with a Sérsic index of 2. In every case we retained all other parameters constant. We show the results in Appendix E. In general, we find that the choices of ϵ , r_{merger} , and DF near the center do not appreciably impact the radial distribution of GCs. Mergers, however, do depend relatively strongly on the choice of these parameters—but are still restricted to no more than a few merger events per simulation ($\lesssim 0.03$ mergers GC^{-1}). In the simulation run with an initially higher central concentration GC distribution we find more mergers ($\lesssim 0.1$ mergers GC^{-1}), without significantly altering our main results.

4.1.2. Method for Comparing with Observations

For each halo and initial GC distribution model, we run 40 simulation realizations. We then compute the average projected distance $\langle r_{\perp} \rangle$ and the number of GCs $\langle N_{\text{GC}} \rangle$ in the final state, splitting the GC sample into mass bins. We report 68% confidence intervals for $\langle r_{\perp} \rangle$ and $\langle N_{\text{GC}} \rangle$; these confidence intervals are dominated by the intrinsic randomness of the finite number of GCs per mass bin (we have verified that the averages and their confidence intervals are stable with respect to increasing the number of realizations per model). The predicted moments $\langle r_{\perp} \rangle$ and $\langle N_{\text{GC}} \rangle$ can then be compared to the observed moments in the data. As noted in Section 3, we only use GC candidates at $r_{\perp} < 2R_e = 3.8 \text{ kpc}$, in order to minimize the background contamination from non-GC sources.

We comment that when GC mergers are not important (the average number of mergers per GC during 10 Gyr is much smaller than unity), the variable N_{GC} simply reflects the observed current number of GCs per mass bin, and does not contain any additional information on the dynamics (apart, of course, from demonstrating the fact that mergers are not important).

5. Results and Discussion

5.1. Results: Observed GC Mass Function as Initial Condition

In this subsection we run the simulations with the observed GC mass distribution as an initial condition; that is, the initial set of GCs is chosen to be identical to the observed set (see Figure 2, correcting only for mass loss). Thus, apart from mergers and mass loss, the only difference between the initial set of GCs and the currently observed set, is the radial distribution. We seek approximate “best-fit” results for each halo model from Section 3, scanning the GCs initial radius and determining agreement with the data by eye. (A more elaborate optimization procedure does not change the results appreciably.) We show the results in Figure 5. In all three models we find reasonable fits to the current GC radial distribution (top row).

The main result of the analysis are the Sérsic radii of the initial GC distribution. These values are indicated in the top row of Figure 5 in the title and the horizontal orange line. For the Stars model, we find $R_e^{(\text{GC})} = 4.5 \text{ kpc}$, significantly more extended than the current distribution of the stellar body. For the Burkert and NFW models we find $R_e^{(\text{GC})} = 2.6$ and 2.5 kpc, respectively, just mildly more extended than the stellar body of UDG1.

We also plot in the top row of Figure 5 an adaptation of Equation (2) corresponding to different models and initial conditions. We set the parameter $\langle r_{0,\perp} \rangle_{\text{core}}$ as the initial average projected distance and the DF time parameter $\tau_{\text{core}}^{(0)} = \tau_{\text{DF}}(r, V_{\text{circ}}(r))|_{R_e=1.9 \text{ kpc}, m_{\text{core}}^{(0)}=5 \times 10^5 M_{\odot}}$ at a reference mass and the half-light radius of the stellar body (recall, the sample of GCs we work with is restricted to $r < 2R_e$). We see that Equation (2) is a useful approximation, in reasonable agreement with the simulations.

In the bottom row of Figure 5 we plot the average number of GCs per mass bin. We find a small number of mergers in all cases $\lesssim 1$ (indicated in the title of the figures). One may notice that even in the absence of mergers (in the Burkert case), the simulation prediction for the number of GCs can be smaller than the initial one. This is the result of masking out GCs at $r_{\perp} > 3.8 \text{ kpc}$ when converting simulation results for comparison with observational data (we present the “initial conditions” number without this cut).

5.2. Results: Almost-as-observed GC Mass Function as Initial Condition

In this subsection we consider an initial set of GC masses that is slightly different than the observed set. This allows us to demonstrate two points. The first point is that a small deficit in the predicted number of GCs in the low- m_{\star} bins, as can be noted in the bottom row of Figure 5, can easily be compensated for by a small increase in the assumed initial number of low-mass GCs. The second point concerns the possibility that GC mergers—rather than pure DF—are the origin of the most-massive few GCs in the observed set. We find that, within the limitations of our simulations, this formation channel for the single most-massive GC may be feasible, although assessing its likelihood in detail is somewhat beyond the expected domain of validity of our method.

We perform this exploration using the NFW halo model. The initial set of GCs is chosen as follows. We break the most-massive GC ($m_{\star} \approx 1.5 \times 10^6 M_{\odot}$) into three GCs, one with

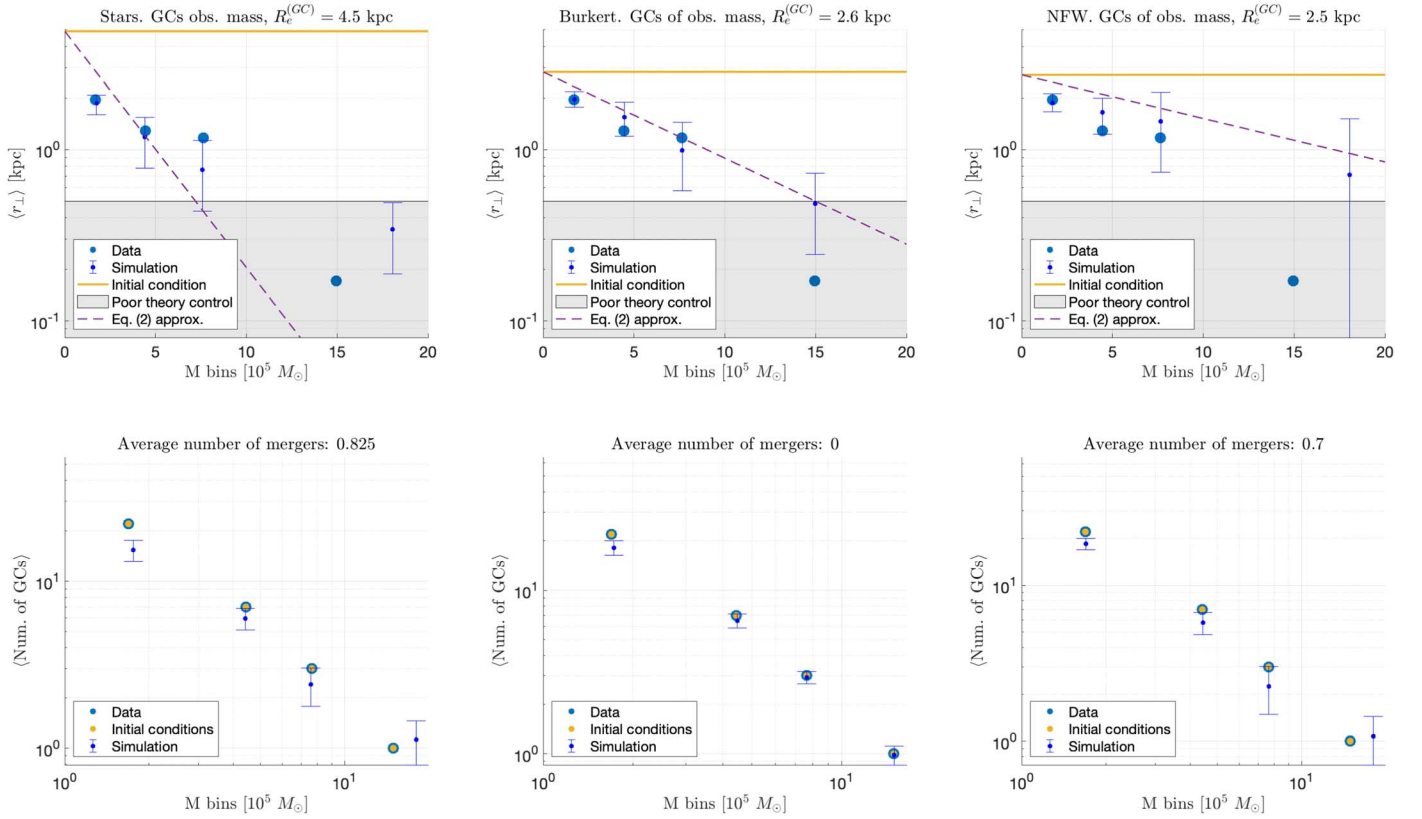


Figure 5. Each column of panels represents a batch of 40 realizations of a halo model and initial conditions. The initial set of GC masses is taken to match the observed set of 33 GCs in Danieli et al. (2022), correcting only for continuous mass loss. The initial radial distribution is Sérsic with $n = 0.61$, with a half-light radius that is different for each halo model. Left column: the Stars model. Middle column: the Burkert model. Right column: the NFW model. Top row: the mean projected radius of GCs in different mass bins. The filled points are data from Danieli et al. (2022; see discussion in 3 and Figure 2). Points with error bars are simulation results including 68% confidence intervals. Horizontal orange lines show the $\langle r_{\perp} \rangle$ of the initial GC distribution (common to all mass bins). The corresponding initial Sérsic radius is $R_e = 4.5, 2.6$, and 2.5 kpc for Stars, Burkert, and NFW, respectively. For comparison, the stellar body of UDG1 is best fit with $R_e \approx 1.9$ kpc, such that $\langle r_{\perp} \rangle \approx 2.1$ kpc. The shaded gray region at $r_{\perp} < 0.5$ kpc is to remind the reader that the predictions of the simulations are least robust in this area, notably because the mass in GCs may not be negligible with respect to the halo enclosed mass (see the text for more details). The dashed purple line is an adaptation of Equation (2) using $\tau_{\text{core}}^{(0)} = \tau_{\text{DF}}(r, V_{\text{circ}}(r))|_{r=R_e}$, $\langle r_{0,\perp} \rangle_{\text{core}}$ calculated using the initial GC distribution. Bottom row: the average number of GCs per mass bin, with big blue points representing the data and medium orange points the initial condition corrected for GC mass loss (by construction for this run, the initial condition is aligned with the data). The small blue points with error bars represent simulation results with the symmetric error estimate $\sigma_N = \sqrt{\langle N_{\text{GC}}^2 \rangle - \langle N_{\text{GC}} \rangle^2}$.

$m_* = 7.5 \times 10^5 M_{\odot}$, and two with $m_* = 3.75 \times 10^5 M_{\odot}$. We also add three light GCs with $M = \{1, 1.75, 2.5\} \times 10^5 M_{\odot}$.

The result of this exercise is shown in Figure 6. We find that (i) the added low-mass GCs in the initial set bring the final set to perfect agreement with observations, and (ii) the simulations do sometimes yield a sufficiently massive most-massive GC, roughly consistent with observations, but this is not common, and happens in only about 20% of the runs. When the most-massive GC is produced by a merger, this merger is essentially always taking place between the second-most-massive GC in the initial state and one of the intermediate m_* GCs.

Both (i) and (ii) above are consequences of the paucity of mergers observed in our simulations. Regarding the low-mass GCs, we expect that the result is quite robust. Regarding the more-massive GCs, since these migrate into the inner halo, where our treatment of DF becomes less trustworthy, it is plausible that our simulations underestimate the massive GC merger rate to some extent. A refined treatment of the dynamics in the inner few 100 pc of the system would be needed to clarify this issue.

5.3. Discussion

The main lesson that we draw from our analysis, analytical and numerical, is that DF provides a natural explanation for the

apparent mass segregation of GCs in UDG1. The projected radial distribution obtained in the simulations is consistent with the trend $\ln \langle r_{\perp} \rangle \propto -m_*$ (see Equation (2) and Figure 3). The slope and intercept of this trend are compatible with simple analytic estimates based on DF theory. The dark matter-dominated halo models are also consistent with independent constraints on the stellar velocity dispersion (Forbes et al. 2021), and suggest a reasonable initial condition for GCs that is only slightly more extended than the current observed stellar body.

We find a low merger rate, $\lesssim 1$ per 10 Gyr (i.e., $\lesssim 3\%$ per GC per 10 Gyr), for all of our halo models. Factors that may, in principle, relax this result include the following: (i) we “turn off” DF in the inner halo, below a radius defined as to guarantee $M_{\text{halo}} \gtrsim M_{\text{GCs}}/2$. Dissipative effects below this radius (~ 0.7 kpc) are not modeled, and could induce more mergers; (ii) our merger criteria may be too strict. We test both of these factors in Appendix E, finding that the results remain fairly robust (especially for dark matter-dominated halo models) even when DF is kept “on” throughout the halo and when the merger criteria are varied.

The few mergers that are observed in the simulations often involve the most-massive GCs, as these both have a larger

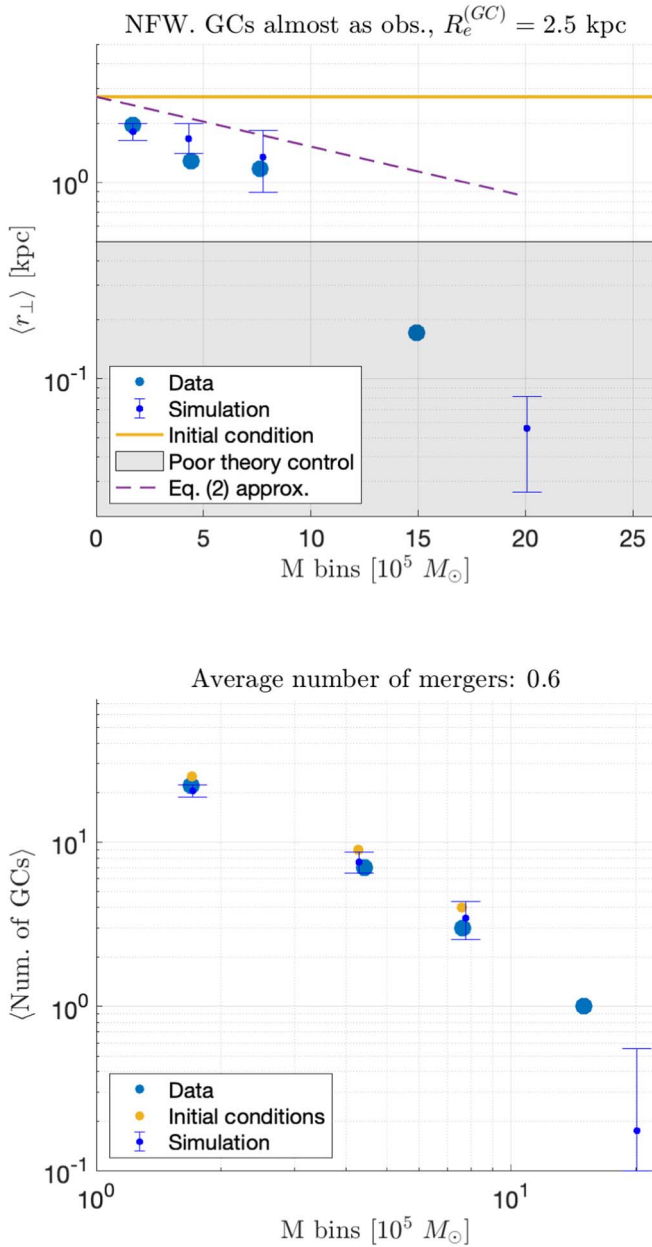


Figure 6. An example where the observed GC mass function is slightly modified: the most-massive GC, of mass $\sim 15 \times 10^5 M_{\odot}$, is traded in the initial GC mass function by one GC with half the mass, and two GCs with one-quarter of the mass. This shows how this massive GC may have been the result of mergers. Additionally, three light GCs with $m_{*} \sim 1.75 \times 10^5 M_{\odot}$ were added to compensate for loss due to the selection of data $r_{\perp} < 3.8$ kpc. Indeed with this addition the simulation is a better fit to the data in the first data point.

intrinsic collision cross section and also settle into the inner halo such that their density is increased. Thus, the occasional mergers observed in the Stars and NFW halo models can slightly skew the initial mass distribution, and with a probability of the order of 20% could even account for the formation of the most-massive GC in the sample through merger.

As a guide for numerical studies, it is possible to analytically estimate the mass of the nuclear cluster m_{nuc} resulting from GC mergers in an NFW halo. Following Bar et al. (2021), we approximate $\tau_{\text{DF}}(r; m_{*}) \approx \bar{\tau}(m_{*}^{(0)}/m_{*})(r/\bar{r})^{\beta}$, applicable for circular orbits with $\beta \approx 2$, and define r_{cr} , the radius below

which GCs on circular orbits decay to the galactic center after time Δt , $r_{\text{cr}}(m_{*}) \approx \bar{r}(4\Delta t(m_{*}/m_{*}^{(0)})/3\tau)^{1/2}$. The nuclear cluster mass is then

$$m_{\text{nuc}} \approx \sum_i m_{*}^{(i)} \int_0^{r_{\text{cr}}(m_{*}^{(i)})} n_{i,0}(r) d^3r, \quad (9)$$

where i runs on GC mass bins and $n_{i,0}$ is the initial GC number density. Using this expression, we find $m_{\text{nuc}} \approx 15 \times 10^5 M_{\odot}$ for the NFW simulation in Figure 5, consistent with the numerical results.

5.4. Caveats and Questionable Simplifications

Before we conclude, we would like to highlight a few possible caveats in our analysis.

1. *Use of semianalytic description of DF.* A semianalytic description of DF has been shown to achieve reasonable agreement with dedicated simulations for a cuspy halo profile (Arca-Sedda & Capuzzo-Dolcetta 2014b; Bar et al. 2021). However, the procedure may be less accurate for cored profiles. It is generally agreed that DF is suppressed near the center of a cored halo (Read et al. 2006; Cole et al. 2012; Kaur & Sridhar 2018; Meadows et al. 2020). However, studies that employ direct numerical simulations do not agree on some details: Cole et al. (2012) and Banik & van den Bosch (2022) report stalling and buoyancy effects at about the core radius, whereas Meadows et al. (2020) reports continued DF, consistent with constant τ_{DF} , and broadly consistent with semianalytic expectations (Petts et al. 2015; Bar et al. 2021).
2. *Merger prescription and tidal disruption.* We neglected the internal dynamics of GCs in the treatment of mergers, and ignored GC tidal disruption by other GCs and by the host halo. Some support for this approximation comes from Dutta Chowdhury et al. (2020), who argued that in a similar setting (NGC1052-DF2) the tidal capture of GCs is not a dominant effect. It would be useful to repeat our calculations using simulations of live GCs, to resolve internal GC dynamics.

We note that disruption of GCs by the halo is unlikely to be important. For circular orbits near the center of an NFW profile, where the effect is most significant, the tidal radius is $r_{\text{tidal}} \approx (m_{*}/M_{200})^{1/3} r_{1/2}^{2/3} R_s^{2/3}$ (Renaud et al. 2011; Orkney et al. 2019). We find for our NFW model $r_{\text{tidal}} \approx 40(r/0.1 \text{ kpc})^{1/3} (m_{*}/10^5 M_{\odot})^{1/3} \text{ pc}$, which is much larger than GC sizes, even when evaluated at a very small radius, 0.1 kpc.

3. *Mass to light ratio.* We assumed a GC mass-to-light (M/L) ratio of $M/L_V = 1.6 M_{\odot}/L_{\odot}$, motivated by Müller et al. (2020) who reported this value, derived from the stacked measured spectra of 11 GCs. Stacking aside, a GC-by-GC analysis suggests a small spread in the mass-to-light ratio ($0.2 M_{\odot}/L_{\odot}$), largely consistent with the 1σ uncertainty of the mass-to-light ratio for the stacked spectra ($1.6^{+0.3}_{-0.1} M_{\odot}/L_{\odot}$). Moreover, most of the GCs in the high-quality sample that we analyzed (22 out of 33) have no spectroscopic data, and thus no direct M/L estimate. Nevertheless, their relatively uniform color (Danieli et al. 2022) suggests they are probably similar to the rest of the GC sample.

A systematic uncertainty in the mass-to-light ratio (either GC-by-GC, or overall) would affect DF estimates, since $\tau_{\text{DF}} \propto 1/m_*$.

4. *Initial conditions.* Our exploration of possible initial conditions for the GC sample was rudimentary, and could be made more systematic. An essential part of the basic preference we find for DF obviously stems from our choice to initiate the GC sample with the same initial radial distribution across GC mass bins; one could, if one wanted, entertain the possibility that DF is ineffective in the system (some models of dark matter, for example, can effectively quench DF; Hui et al. 2017; Bar et al. 2021), and that for some reason, more-massive GCs are preferentially formed deeper into the host halo compared to less-massive GCs, in a formation pattern that mimics the natural expectations from DF. Indeed, galaxy formation simulations may indicate that more-massive GCs form closer to the center of galaxies (Reina-Campos et al. 2021).

Another concrete example for a mechanism that could also induce GC mass segregation was briefly discussed in Section 2.3: if the total mass of UDG1 was dominated by GCs during a brief ($\mathcal{O}(100 \text{ Myr})$) early epoch before substantial GC mass loss took place, and under the (perhaps highly simplified) assumption that GCs formed at the same time, two-body relaxation of the GCs could have contributed to the mass segregation. This would essentially amount to mass segregation in initial conditions, since we do not attempt to model this epoch within our simulations.

We stress that the DF within our models is an irreducible effect. It should contribute to mass segregation also in the scenario of initial mass segregation. We note, however, that this expectation may spoil in the case of a high merger rate.

5. *Galaxy mergers.* We did not consider the possibility that UDG1 has undergone mergers with other galaxies.
6. *Tidal stripping.* Likely a member of NGC5846 galaxy group (Müller et al. 2020; Danieli et al. 2022), UDG1 may have been affected by tidal forces. Taking as a benchmark the near galaxy NGC5846 and the distance assumption of 26.5 Mpc, the two galaxies are separated by projected distance $r_{\text{gal}} = 164 \text{ kpc}$. Taking this as an estimate for the true distance between the galaxies, the tidal radius is

$$r_{\text{tidal}} \approx r_{\text{gal}} \left(\frac{M_{\text{UDG1}}}{2M_{\text{NGC5846}}} \right)^{1/3} \\ = 6 \left(\frac{M_{\text{UDG1}}}{10^8 M_{\odot}} \right)^{1/3} \left(\frac{10^{12} M_{\odot}}{M_{\text{NGC5846}}} \right)^{1/3} \text{ kpc}. \quad (10)$$

Here, the reference value for the mass of UDG1 is on the low side, neglecting any contribution from dark matter; thus, it is relevant for the **Stars** model. For the mass of NGC5846, we used $10^{12} M_{\odot}$. We see that the GC initial condition found for the **Stars** model (half-mass radius of 4.5 kpc) may indicate some level of inconsistency with the tidal radius estimate. The dark matter-dominated halo models (NFW and Burkert) seem conveniently compatible with the tidal radius—although the halos themselves may be somewhat affected by tidal stripping.

6. Summary

We have shown that the observed radial distribution of GCs in NGC5846-UDG1 is suggestive of mass segregation. The mass segregation pattern can naturally be explained by DF. While the basic imprint of DF appears clear, uncertainties on the initial distribution of GCs at formation complicate the task of drawing robust constraints on the dark matter content of the halo. Assuming that GCs form at a characteristic radius that is not widely different from that of the bulk of the stellar population (not in GCs), and that the characteristic GC formation radius does not depend on GC birth mass, the data provides dynamical support for a massive dark matter-dominated halo for UDG1. This demonstrates that dynamical arguments (and not only kinematics) can shed light on the distribution of dark matter in galaxies.

The dynamical preference for a massive halo can be further tested with kinematics data. Indeed, it is broadly consistent with existing kinematics results from Forbes et al. (2021).

Our study motivates, and can benefit from, several technical improvements in the scope and detail of our numerical simulations, as noted in the main text. Input from the theory of the formation of GCs, their expected mass function at birth and their initial characteristic radial scale (especially in comparison with the main stellar system), could provide better-informed priors for the initial conditions, allowing the dynamics analysis to produce sharper constraints on the dark matter halo. Alternatively, a more detailed phenomenological scrutiny of GC initial conditions in UDG1 may be useful to inform GC formation theory, especially if combined with kinematics constraints.

More observational studies of UDG1-like galaxies, where GCs at various masses can be reliably identified and characterized, will play an important role in future work of this kind. The large sky coverage and point-source depth of the upcoming Vera Rubin Observatory Legacy Survey of Space and Time (LSST Science Collaboration et al. 2009) will enable mapping of GCs associated with low surface brightness galaxies in the nearby universe. Looking ahead, the Nancy Grace Roman Space Telescope (Spergel et al. 2015) will open an unprecedented window into studies of extragalactic GCs. Its wide-field imaging, high spatial resolution, and sensitivity will allow probing GCs below the turnover magnitude across the sky and out to larger distances.

We thank Diederik Kruijssen, Shaunak Modak, Aaron Romanowsky, Scott Tremaine, Sebastian Trujillo Gomez, and Pieter van Dokkum for comments on the manuscript and Boaz Katz and Karamveer Kaur for useful discussions. We thank Oliver Müller for a useful discussion on the spectroscopy of UDG1. We are also grateful to the anonymous reviewer for useful suggestions that improved the manuscript. N.B. is grateful for the support of the Clore scholarship of the Clore Israel Foundation. K.B. and N.B. were supported by grant 1784/20 from the Israel Science Foundation. S.D. is supported by NASA through Hubble Fellowship grant HST-HF2-51454.001-A awarded by the Space Telescope Science Institute, which is operated by the Association of Universities for Research in Astronomy, Incorporated, under NASA contract NAS5-26555.

Appendix A

Robustness of the GC Sample and Mass Segregation

It is important to substantiate that our results are not sensitive to the photometric selection criteria of Danieli et al. (2022). Figure 1 demonstrates that our sample ($m_V < 25.0$ mag) is expected to be contaminated by one object at the low-luminosity end. Therefore contamination is very unlikely to change the results.

Another risk of using photometric selection criteria is the potential oversight of true GCs. To test this possibility, we re-examine the data presented in Danieli et al. (2022) by generously relaxing the selection criteria: changing the FWHM size and color from $2.4 < \text{FWHM} < 4.5$ pix ($2.1 < \text{FWHM} < 4.5$ pix) and $0.2 < \text{F475W} - \text{F606W} < 0.6$ ($0.08 < \text{F475W} - \text{F606W} < 0.8$) for $m_V < 24.5$ mag ($24.5 < m_V < 25$ mag) to $1.0 < \text{FWHM} < 10.0$ pix and $0 < \text{F475W} - \text{F606W} < 1$. This new sample is shown in Figure 7, after masking two bright objects whose spectroscopy suggests nonmembership with UDG1 (Müller et al. 2020).¹¹ Relaxing the selection criteria, nine new objects are added (whose would-be luminosities are estimated assuming distance to UDG1): (i) eight out of the nine are relatively faint objects at large radii, consistent with a contamination of 12 objects by comparing to a nearby background field; (ii) a very red and bright object with a color of $\text{F475W} - \text{F606W} = 0.98$ mag. It is suggestive to compare this to the 11 spectroscopically confirmed GCs (which have similar brightness) and are narrowly distributed at $\text{F475W} - \text{F606W} = 0.39$ mag with a standard deviation of 0.03 mag. Due to this large difference, we assume this object to be foreground. We note that it is difficult to substantiate spectroscopically as this object is very near on the sky to a very bright foreground star.

It is also important to quantify the significance of the mass segregation trend, argued in Figure 2. To that end, we generate a mock sample of GCs from a common radial distribution—exactly

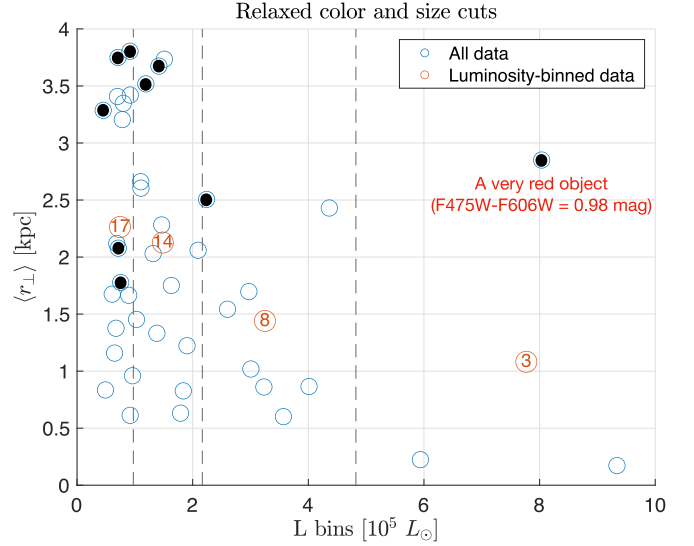


Figure 7. A modified GC sample with relaxed photometric selection criteria, as explained in the text. The “very red object” refers to an object whose color ($\text{F475W} - \text{F606W} = 0.98$ mag) differs by about 20 standard deviations than similar other spectroscopically confirmed GCs ($\text{F475W} - \text{F606W} = 0.39 \pm 0.03$ mag).

like our simulations setup (Section 4). We carry out two exercises with this mock data. First (Figure 8, left), we show an example of the radii of GCs versus their mass, as in Figure 5, showing that the no-mass-segregation hypothesis is not compatible with the data, in comparison to the models shown in the paper. Second, we define a test statistic that is a good proxy to mass segregation: the slope of the line in $\log(r_\perp)$ versus m_* . We show a histogram of this test statistic for the mock data. We estimate from this a p -value $\lesssim 1\%$ for the hypothesis that the data contains no mass segregation. These exercises support our claim of a mass segregation trend in the data of UDG1.

¹¹ We thank Oliver Müller for help on this point.

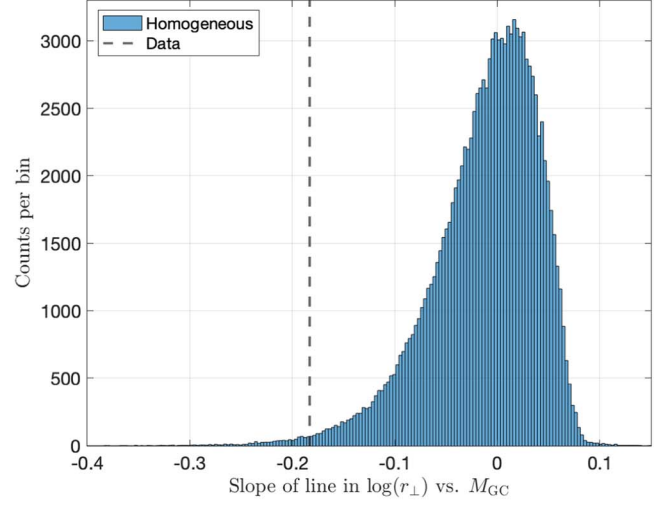
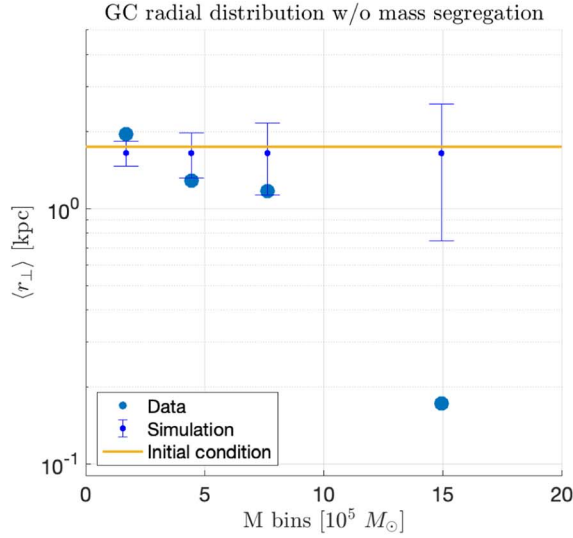


Figure 8. Left: the same as upper panels of Figure 5, for a “simulation” that is the mock GC data discussed in the text—without any time integration—such that it presents no mass segregation. Right: a histogram of the slope of line in $\log(r_{\perp})$ vs. m_{*} —a test statistic μ , essentially—for mock data of GCs in UDG1 all drawn from the same radial distribution (“homogeneous”). The vertical dashed line shows this test statistic for the data (μ_{data}) of UDG1. The probability $p(\mu < \mu_{data}) = 0.008$.

Appendix B

Two-body Relaxation of GCs in a Background Potential

The classic two-body relaxation timescale of a self-gravitating system can be extended to the case of an N -body system in an external potential, following Binney & Tremaine (2008). Assume N GCs, each with a mass m spread along a characteristic radius R with a characteristic velocity v induced by a body of mass $M_{tot} = Rv^2/G$. The mean square change in velocity per crossing time is then

$$\begin{aligned} \Delta v^2 &\approx 8N \left(\frac{Gm}{Rv} \right)^2 \ln \Lambda = 8N \left(\frac{m}{M_{tot}} \right)^2 v^2 \ln \Lambda \\ &= \frac{8}{N} \left(\frac{Nm}{M_{tot}} \right)^2 v^2 \ln \Lambda. \end{aligned} \quad (B1)$$

Defining $f \equiv Nm/M_{tot} = M_{GCs}/M_{tot}$ (likely $\sim 0.01 \div 0.1$ for the example of UDG1) and using $\ln \Lambda = \ln R/b_{90}$, with b_{90} being the impact factor parameter where a mass is deflected by 90° , i.e., $b_{90} = 2Gm/v^2$, one finds $\ln \Lambda = \ln(N/f)$. We therefore obtain

$$\Delta v^2 = \frac{8}{N} f^2 v^2 \ln \frac{N}{f}. \quad (B2)$$

The relaxation time is

$$t_{relax} \sim t_{cross} N_{cross} \approx t_{cross} \frac{v^2}{\Delta v^2} \approx \frac{0.1N}{\ln \frac{N}{f}} \frac{1}{f^2} t_{cross}, \quad (B3)$$

where $t_{cross} \sim R/v$.

For a UDG with $v \sim 10 \text{ km s}^{-1}$ and $r \sim 2 \text{ kpc}$, $t_{cross} \sim 0.2 \text{ Gyr}$, one finds

$$t_{relax} \sim 10 \left(\frac{N}{30} \right) \left(\frac{R}{2 \text{ kpc}} \right) \left(\frac{10 \text{ km s}^{-1}}{v} \right) \left(\frac{0.1}{f} \right)^2 \text{ Gyr}. \quad (B4)$$

(It is possible to replace $f = Nm/M_{tot} = NmG/(Rv^2)$, which changes dependencies on variables.)

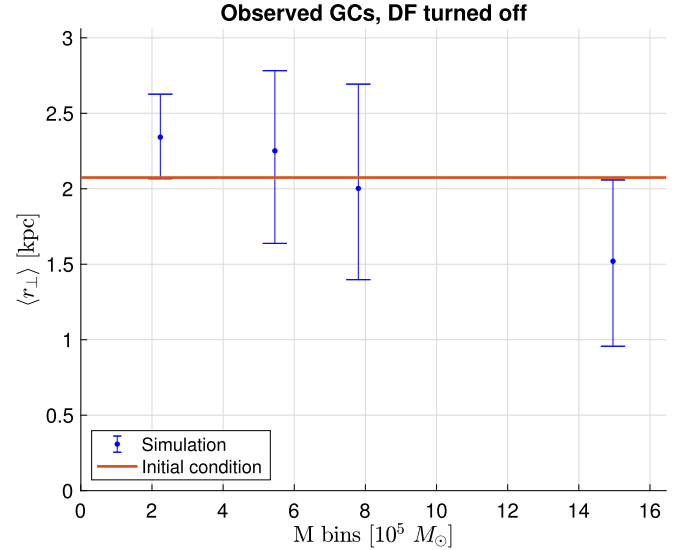


Figure 9. A simulation batch where dynamical friction is turned off, using the Stars model, as explained in Section 3. The interaction between GCs causes the mass segregation. Of course, the segregation depends on the GC mass function, which we take to be the sample of 33 observed GCs (Danieli et al. 2022).

We find the interesting result that two-body relaxation of GCs is marginally effective in a galaxy such as NGC5846-UDG1, in the case where its dynamics is dominated by the observed stellar body. Indeed, we find support for these estimates in an N -body simulation where external dynamical friction is turned off (see Figure 9). Unsurprisingly, more-massive GCs sink to small radii whereas lighter GCs experience a “buoyancy”-like effect. This should be kept in mind: while lighter constituents (stars and dark matter) of the galaxy mostly operate as friction, the GC distribution works both as friction and as heating. Of course, this effect is only appreciable in light-mass models such as the Stars model.

Appendix C Projection Effects

The expectation value of the projected distances can be re-expressed as

$$\begin{aligned}\langle r_{\perp} \rangle &= \int d^3r n(r) r_{\perp} = 2\pi \int dr r^2 n(r) \sin \theta \sin \theta d\theta \\ &= \frac{\pi^2}{2} \int dr r^2 n(r) = \frac{\pi}{4} \langle r \rangle,\end{aligned}\quad (C1)$$

where we assumed spherical symmetry.

For a single GC, taking a circular orbit with radius r for simplicity, the time-average expected projected radius is

$$\langle r_{\perp} \rangle_t = \frac{1}{T} \int_0^T r \sin(\omega t) dt = \frac{\pi}{2} r. \quad (C2)$$

This is of course only a crude estimate. We may do better by using simulation data. Taking the last 1 Gyr of $r(t)$ and $r_{\perp}(t)$ of different simulations and mass models, we find (subscript t denotes averaging over time)

$$\langle r_{\perp} \rangle_t \approx 0.8 \langle r \rangle_t. \quad (C3)$$

Indeed, this agrees with the estimates used in the literature, e.g., $r_{\perp} \approx (\sqrt{3}/2)r$ and $r_{\perp} \approx (3/4)r$ in Hui et al. (2017) and Meadows et al. (2020), respectively.

Appendix D Faintest Objects Set

Below a luminosity threshold corresponding magnitude $m_V \approx 25$, there is considerable contamination of other sources in the field of view of the galaxy (Danieli et al. 2022). In the selection criteria of Danieli et al. (2022), the lowest luminosity set contains 43 objects, whereas a nearby background sample with 6.5 times more area contains $k_0 = 155$ sources—or about 24 objects per galactic-area, implying $\mathcal{O}(1)$ contamination in that low-luminosity set. In order to nevertheless extract information about the radial distribution of true GCs in this set, we first divide the galaxy into radial bins of area $S_{\text{bin}}^{(i)}$. When the background area $S_{\text{bg}} \gg S_{\text{bin}}^{(i)}$, the expected background objects per bin is $\lambda_i \approx k_0 \times S_{\text{bin}}^{(i)} / S_{\text{bg}}$. Assuming the background is Poisson-distributed, we can estimate the true number of objects in a given bin. In the current work, we refrain from a full statistical analysis, which would require a more careful treatment and modeling of the statistical distribution of true GCs. Instead,

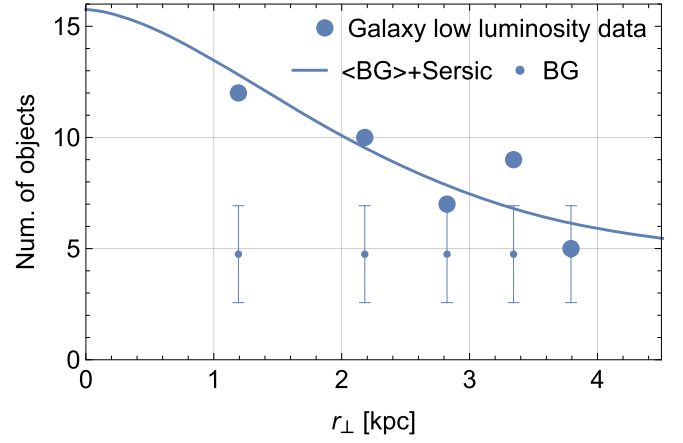


Figure 10. Thick points are the number of objects in the lowest luminosity sample of Danieli et al. (2022) per radial bin. The projected radius is taken as $\langle r_{\perp} \rangle = \int_{r_1}^{r_2} \Sigma(r_{\perp}) r_{\perp} d^2 r_{\perp} / \int_{r_1}^{r_2} \Sigma(r_{\perp}) d^2 r_{\perp} \approx (2/3)(r_2^3 - r_1^3) / (r_2^2 - r_1^2)$, taking $\Sigma \approx \text{constant}$ per bin with r_1 and r_2 inner and outer radii of each bin. The contamination background (BG) is shown in points with error bars \pm standard deviation. The contamination is universal among different bins because we chose the bins to have an equal area. The solid line is the sum of the expected contamination ($\langle \text{BG} \rangle$) and a Sérsic profile with $n = 0.61$ and $R_e = 2.3$ kpc, slightly more extended than the Stars in UDG1 (since bins are of equal area, the Sérsic surface density can be adopted immediately).

we plot in Figure 10 the data along with contamination per radial bin and demonstrate that a Sérsic profile in the ballpark of the Stars distribution is a good fit to the data.

Appendix E Further Simulations

In this Appendix we demonstrate the sensitivity of our results in Figure 5 under the change of several modeling choices that we made in Section 4. In Figure 11 we show the simulations without the restriction of DF at $r < 0.3R_e$ and $M_{\text{halo}} - M_{\text{GCs}}/2 < 0$. Namely, in producing this plot, we let DF remain active throughout the halo. In Figure 12 we show the results of simulations for different values of the GC Plummer softening parameter ϵ . In Figure 13 we show the results of simulations for different values of the critical merger radius r_{merger} . In Figure 14 we show the results of simulations for a more centrally concentrated initial distribution of GCs, using a Sérsic index $n_{\text{GC}} = 2$.

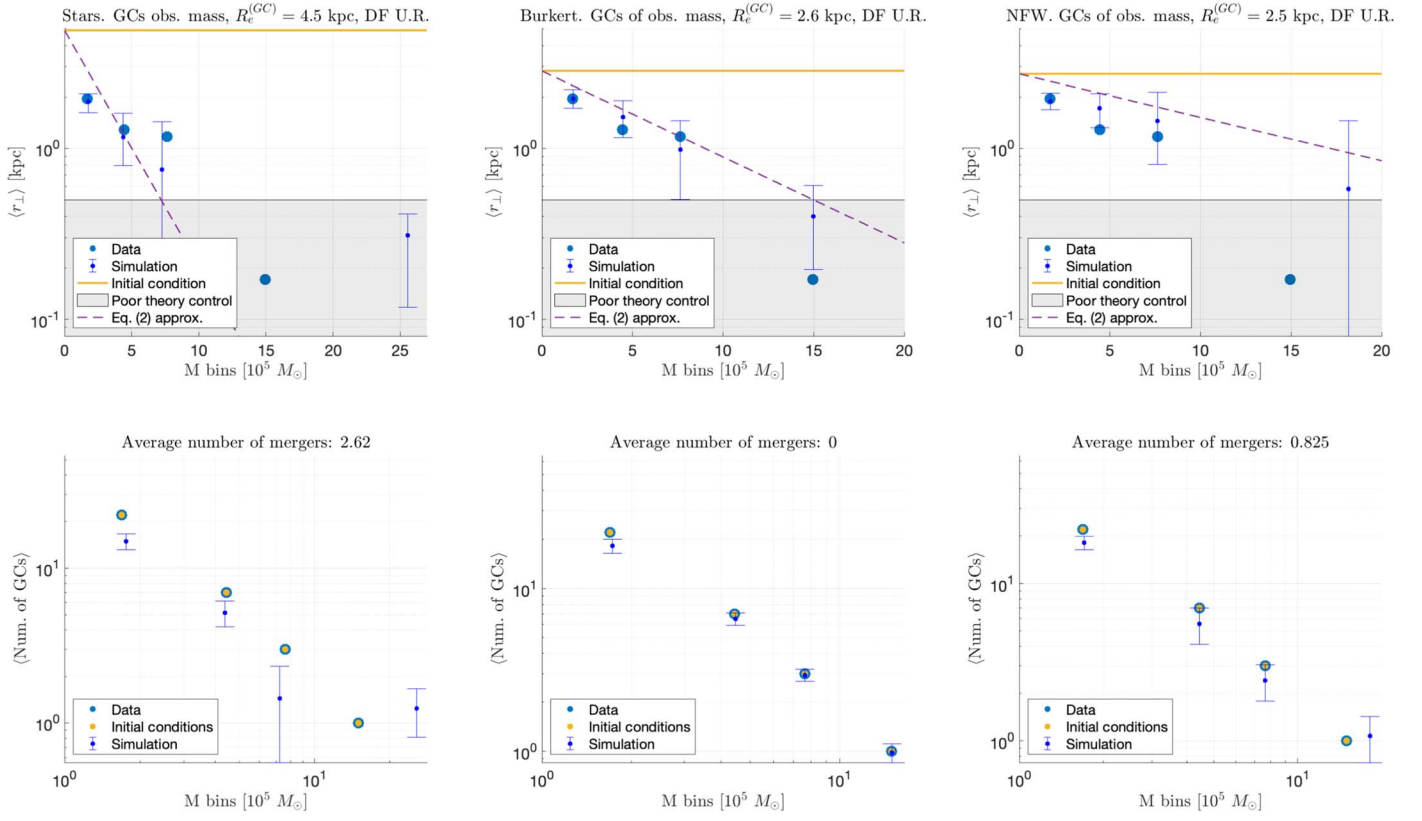
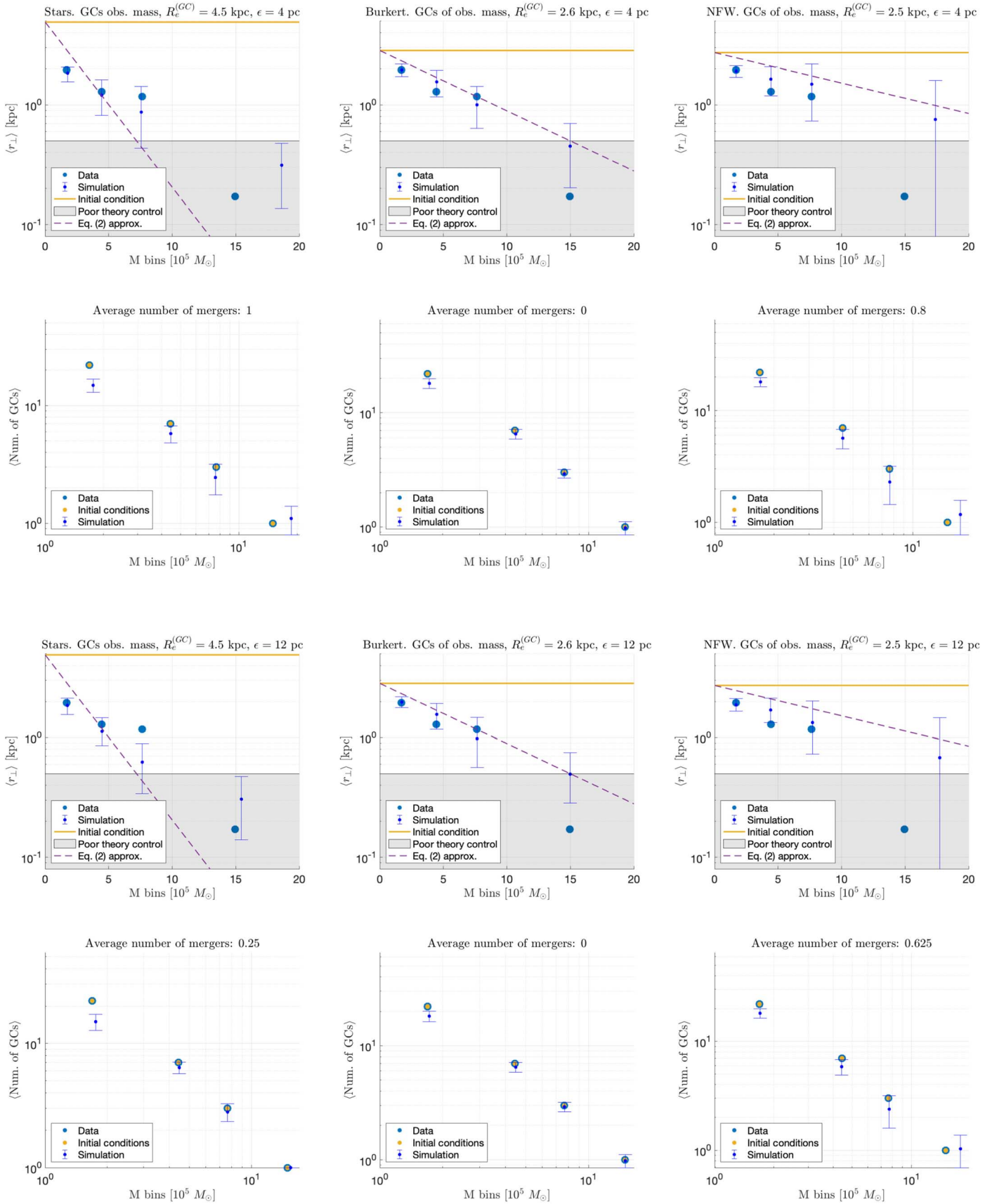
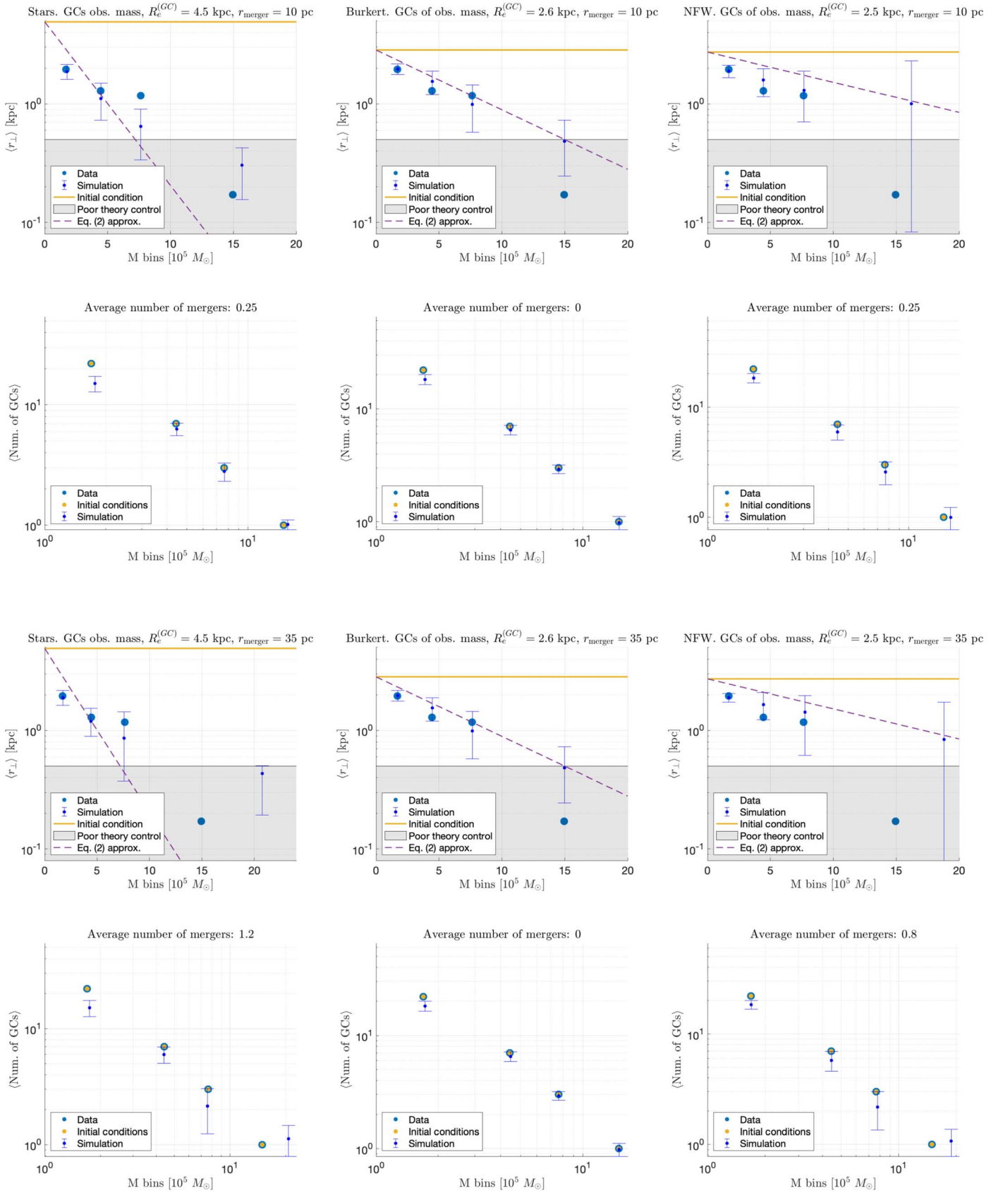


Figure 11. Like Figure 5, but with unregulated DF (“DF U.R.”), i.e., without turning off DF at any radius, either due to core stalling conditions $r < 0.3R_e$ or the enclosed mass condition $M_{\text{halo}} - M_{\text{GCs}}/2 < 0$.

Figure 12. Like Figure 5, but $\epsilon = 4$ pc (top) and $\epsilon = 12$ pc (bottom).

Figure 13. Like Figure 5, but $r_{\text{merger}} = 10$ pc (top) and $r_{\text{merger}} = 35$ pc (bottom).

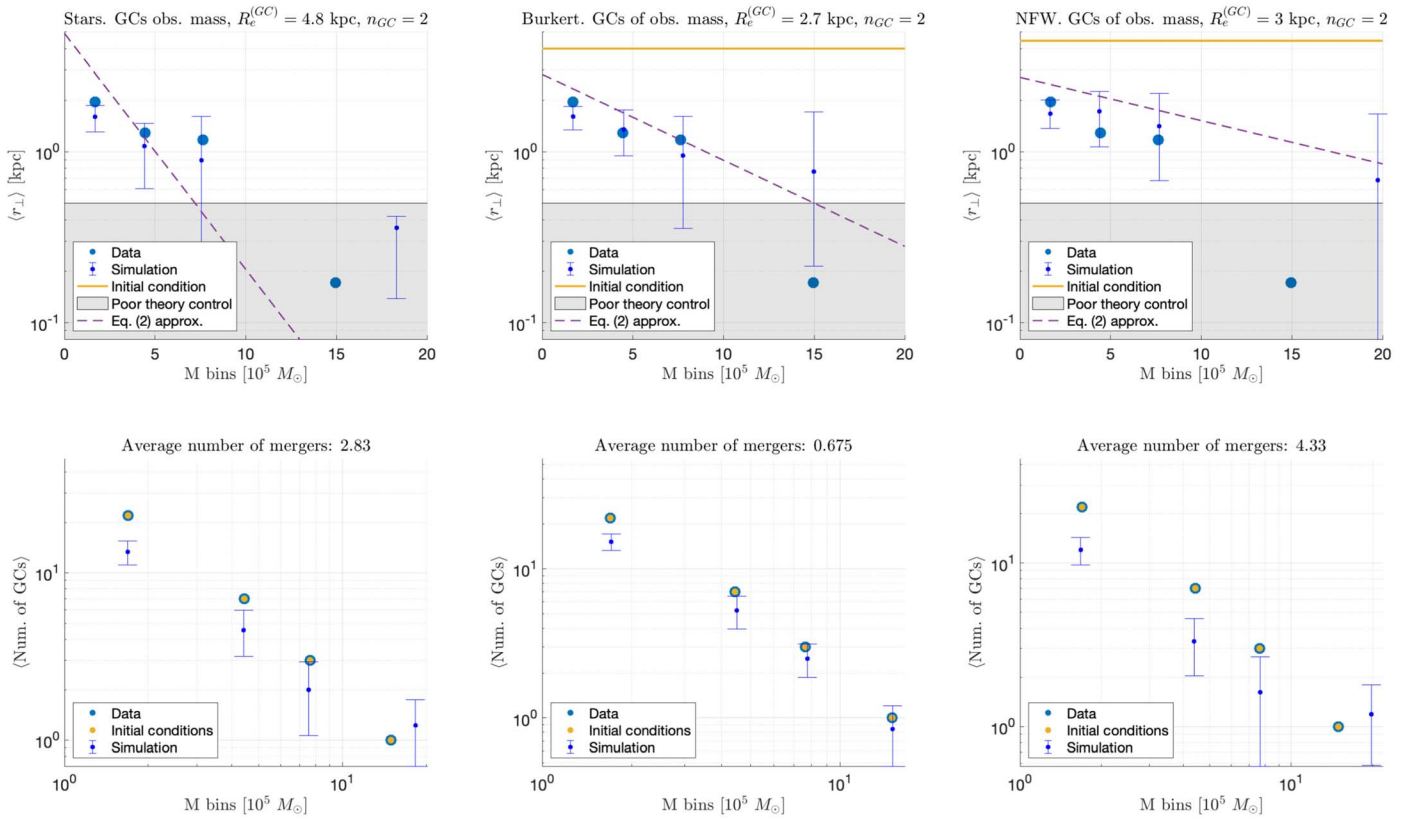


Figure 14. Like Figure 5, but with $n_{GC} = 2$, i.e., a relatively cuspy GC distribution.

ORCID iDs

Nitsan Bar <https://orcid.org/0000-0002-3724-5082>
 Shany Danieli <https://orcid.org/0000-0002-1841-2252>
 Kfir Blum <https://orcid.org/0000-0001-8978-5155>

References

- Arca-Sedda, M., & Capuzzo-Dolcetta, R. 2014a, *MNRAS*, **444**, 3738
 Arca-Sedda, M., & Capuzzo-Dolcetta, R. 2014b, *ApJ*, **785**, 51
 Banik, U., & van den Bosch, F. C. 2022, *ApJ*, **926**, 215
 Bar, N., Blas, D., Blum, K., & Kim, H. 2021, *PhRvD*, **104**, 043021
 Bar-Or, B., Fouvy, J.-B., & Tremaine, S. 2019, *ApJ*, **871**, 28
 Binney, J., & Tremaine, S. 2008, *Galactic Dynamics: Second Edition* (Princeton, NJ: Princeton Univ. Press)
 Boldrini, P., Mohayaee, R., & Silk, J. 2020, *MNRAS*, **492**, 3169
 Burkert, A. 1995, *ApJL*, **447**, L25
 Cappellari, M., Emsellem, E., Krajnović, D., et al. 2011, *MNRAS*, **413**, 813
 Capuzzo-Dolcetta, R. 1993, *ApJ*, **415**, 616
 Capuzzo-Dolcetta, R., & Tesserì, A. 1997, *MNRAS*, **292**, 808
 Chandrasekhar, S. 1943, *ApJ*, **97**, 255
 Cole, D. R., Dehnen, W., Read, J. I., & Wilkinson, M. I. 2012, *MNRAS*, **426**, 601
 Danieli, S., van Dokkum, P., Trujillo-Gomez, S., et al. 2022, *ApJL*, **927**, L28
 Dutta Chowdhury, D., van den Bosch, F. C., & van Dokkum, P. 2019, *ApJ*, **877**, 133
 Dutta Chowdhury, D., van den Bosch, F. C., & van Dokkum, P. 2020, *ApJ*, **903**, 149
 Forbes, D. A., Gannon, J., Couch, W. J., et al. 2019, *A&A*, **626**, A66
 Forbes, D. A., Gannon, J. S., Romanowsky, A. J., et al. 2021, *MNRAS*, **500**, 1279
 Gnedin, O. Y., Ostriker, J. P., & Tremaine, S. 2014, *ApJ*, **785**, 71
 Goerdt, T., Moore, B., Read, J. I., Stadel, J., & Zemp, M. 2006, *MNRAS*, **368**, 1073
 Hernandez, X., Matos, T., Sussman, R. A., & Verbin, Y. 2004, *PhRvD*, **70**, 043537
 Hui, L., Ostriker, J. P., Tremaine, S., & Witten, E. 2017, *PhRvD*, **95**, 043541
 Kaur, K., & Sridhar, S. 2018, *ApJ*, **868**, 134
 Kourkchi, E., & Tully, R. B. 2017, *ApJ*, **843**, 16
 Krumholz, M. R., McKee, C. F., & Bland-Hawthorn, J. 2019, *ARA&A*, **57**, 227
 Lim, S., Peng, E. W., Côté, P., et al. 2018, *ApJ*, **862**, 82
 Lotz, J. M., Telford, R., Ferguson, H. C., et al. 2001, *ApJ*, **552**, 572
 LSST Science Collaboration, Abell, P. A., Allison, J., et al. 2009, arXiv:0912.0201
 Magni, S. 2015, PhD thesis, Université de Montpellier, <https://orilu.uni.lu/handle/10993/36585>
 Meadows, N., Navarro, J. F., Santos-Santos, I., Benítez-Llambay, A., & Frenk, C. 2020, *MNRAS*, **491**, 3336
 Müller, O., Durrell, P. R., Marleau, F. R., et al. 2021, *ApJ*, **923**, 9
 Müller, O., Marleau, F. R., Duc, P.-A., et al. 2020, *A&A*, **640**, A106
 Navarro, J. F., Frenk, C. S., & White, S. D. M. 1997, *ApJ*, **490**, 493
 Nusser, A. 2018, *ApJL*, **863**, L17
 Oh, K. S., Lin, D. N. C., & Richer, H. B. 2000, *ApJ*, **531**, 727
 Orkney, M. D. A., Read, J. I., Petts, J. A., & Gieles, M. 2019, *MNRAS*, **488**, 2977
 Ostriker, J. P., & Gnedin, O. Y. 1997, *ApJ*, **487**, 667
 Pedcenko, A. 2020, N-body simulation with ode45 v1.0.5, MATLAB Central File Exchange, <https://www.mathworks.com/matlabcentral/fileexchange/75202-n-body-simulation-with-ode45>
 Petts, J. A., Gualandris, A., & Read, J. I. 2015, *MNRAS*, **454**, 3778
 Read, J. I., Goerdt, T., Moore, B., et al. 2006, *MNRAS*, **373**, 1451
 Reina-Campos, M., Trujillo-Gomez, S., Deason, A. J., et al. 2021, arXiv:2106.07652
 Renaud, F., Gieles, M., & Boily, C. M. 2011, *MNRAS*, **418**, 759
 Sánchez-Salcedo, F. J., & Lora, V. 2022, *MNRAS*, **511**, 1860
 Sanchez-Salcedo, F. J., Reyes-Iturbide, J., & Hernandez, X. 2006, *MNRAS*, **370**, 1829
 Shao, S., Cautun, M., Frenk, C. S., et al. 2021, *MNRAS*, **507**, 2339
 Shen, Z., van Dokkum, P., & Danieli, S. 2021, *ApJ*, **909**, 179
 Spergel, D., Gehrels, N., Baltay, C., et al. 2015, arXiv:1503.03757
 Tremaine, S. 1976, *ApJ*, **203**, 345
 Tremaine, S. D., Ostriker, J. P., & Spitzer, L. J. 1975, *ApJ*, **196**, 407
 van Dokkum, P., Abraham, R., Romanowsky, A. J., et al. 2017, *ApJL*, **844**, L11
 van Dokkum, P., Cohen, Y., Danieli, S., et al. 2018, *ApJL*, **856**, L30